EXPERIMENTAL STUDIES AND SIMULATIONS OF HYDROGEN PELLET ABLATION IN THE STELLARATOR TJ – II

N. Panadero[1], K. J. McCarthy[1], F. Koechl[2,3], J. Baldzuhn[4], J. L. Velasco[1], S. K. Combs[5], E. de la Cal[1], R. García[1], J. Hernández Sánchez[1], D. Silvagni[6], Y. Turkin[4], TJ-II team and W7-X team

1. Laboratorio Nacional de Fusión, CIEMAT, Madrid, Spain

2. Atominstitut, Technische Universität Wien, Vienna, Austria

3. Culham Centre for Fusion Energy, Culham Science Centre, Abingdon, OX14 3DB, Oxfordshire, UK

4. Max-Planck-Institut für Plasmaphysik, Greifswald, Germany

5. Fusion & Materials for Nuclear Systems Division, ORNL, Tennessee, USA

6. Universidad Carlos III de Madrid, Leganés, Spain

E-mail: nerea.panadero@ciemat.es

Abstract. Plasma core fuelling is a key issue for the development of steady-state scenarios in large magnetically-confined fusion devices, in particular for helical-type machines. At present, cryogenic pellet injection is the most promising technique for efficient fuelling. Here, pellet ablation and fuelling efficiency experiments, using a compact pellet injector, are carried out in Electron Cyclotron Resonance and Neutral Beam Injection heated plasmas of the stellarator TJ-II. Ablation profiles are reconstructed from light emissions collected by silicon photodiodes and a fast-frame camera system, under the assumptions that such emissions are loosely related to the ablation rate and that pellet radial acceleration is negligible. In addition, pellet particle deposition and fuelling efficiency are determined using density profiles provided by a Thomson Scattering system. Furthermore, experimental results are compared with ablation and deposition profiles provided by the HPI2 pellet code, which is adapted here for the stellarators Wendelstein 7–X (W7-X) and TJ-II. Finally, the HPI2 code is used to simulate ablation and deposition profiles for pellets of different sizes and velocities injected into relevant W7–X plasma scenarios, while estimating the plasmoid drift and the fuelling efficiency of injections made from two W7–X ports.

1. Introduction

Plasma core fuelling is one of the key issues for the development of steady-state operation in large magnetically-confined plasma fusion devices. This is of particular importance for helical-type machines since neoclassical theory predicts that on-axis Electron Cyclotron Resonance Heating (ECRH) requires a particle source with the same radial profile to mitigate potential core particle depletion [1]. The current standard method for fuelling, gas injection, is predicted to be inefficient for large devices since the particle source is located at the plasma edge [2]. Hence, the most promising technique for plasma core fuelling is cryogenic pellet injection. Given that fuel is deposited well inside the last-closed flux-surface (LCFS) of the confined plasma, fuelling should increase. Moreover, this particle source does not have an associated energy source unlike Neutral Beam Injection (NBI) [2].

Cryogenic pellet technology is a well-developed technology that has been employed on numerous medium- and large-sized fusion devices for several decades [3]. Indeed, numerous experimental studies have been carried out, both in tokamaks and stellarators, during this time [3]. One of the most relevant findings, in particular for this work, was the identification of the displacement of the ablated material along the magnetic field gradient [4, 5]. Nonetheless, it should be noted that the interpretation of experimental results is more difficult for stellarators due to the complexity of their magnetic fields [3]; hence there remains a need to undertake further studies for this type of device.

At present, experimental penetration depths and ablation rates are well reproduced by ablation models [6–12], some of which consider the anisotropic effects associated with the confining magnetic field [10–12], *e.g.*, the latter references [11, 12] are 2-D. Moreover, regarding plasma density evolution, *i.e.*, particle deposition, a number of models include an **ExB** drift of the ablated material to explain the discrepancy between ablation and deposition profiles, where the electric field, **E**, is produced by the acceleration of plasmoid charged particles in the background inhomogeneous magnetic field [13]. In addition, several mechanisms that either enhance [14] or reduce [13, 15, 16] such a drift have been proposed. These models can reproduce accurately the experimental results in tokamaks [3, 17, 18]. For instance, these drift effects are included in the Hydrogen Pellet Injection (HPI2) code, developed by Pégourié and Köchl [10, 13, 19]. The HPI2 is the reference code for pellet simulations in tokamaks since it allows simulating both the ablation of the pellet and the homogenization of the ablated material in a self-consistent way. Indeed, pellet injection has been simulated in several tokamaks using the HPI2 code, such as JET [20, 21], MAST [22] or Tore Supra [23], reproducing closely the experimental results, even though the homogenization model used assumes spatially homogeneous plasmoid characteristics and heating, a limitation that is partially removed in more self-consistent 1-D models [11], [12]. In addition, it has been used for theoretical studies and design proposals for ITER and DEMO [19, 24–27].

In contrast, the situation is different for stellarators. To date, the HPI2 code has only been adapted for the Large Helical Device (LHD) [28, 29]. However, it was found from experimental results that pellet injections are qualitatively different from what is obtained for tokamaks, since the favourable inward drift detected for HFS injections in

other devices is not observed in LHD [30, 31]. This situation is not fully understood; thus, further theoretical, simulation and experimental work is necessary for LHD. One current, and rather urgent, task is the adaption and benchmarking of the HPI2 for the recently commissioned W7-X device. This is critical given that pellet injection will be an essential tool to achieve its scientific goal of steady-state operation at high densities and thereby demonstrate the viability of stellarators as future fusion reactors [32]. In order to begin this work, simulations are needed to understand and quantify the influence of pellet size and velocity, of plasma parameters, such as density, temperature, magnetic configuration or heating method, and of injection location on pellet penetration, ablated material deposition and fuelling efficiency, and hence optimize injections. For this, a prior validation of a W7-X version of the HPI2 code is needed. One means of undertaking this is to adapt the same code to the medium-sized stellarator TJ-II on which a pellet injector has been operated since mid-2014 [33–35]. The large pellet injection database of TJ-II can then be used to benchmark the W7-X version. Such benchmarking, despite the device size and plasma parameter differences, is considered valid since the underlying drift mechanisms, related to the non-axisymmetry of the magnetic configuration, are equivalent.

In this work, after summarizing the pellet ablation and deposition code, the modifications made to a version developed for tokamaks, for its adaptation to the W7-X and TJ-II stellarators, are outlined and explained. Next, hydrogen pellet ablation studies performed on the TJ-II are described and comparisons are made between experimental results and HPI2 simulations. Further on, ablation and deposition profiles are calculated for the optimized stellarator W7–X [36], on which a pellet injector will be installed for the second phase of operation. Finally, the findings are discussed, conclusions are drawn with regard to the viability of this code for stellarators, and recommendations are made for pellet studies on the W7-X.

2. Background

A cryogenic pellet injected into high temperature plasma is exposed to the incident energetic particles of background plasma that ablate it until it is completely consumed. Subsequent to ablation, the ablated pellet material is homogenized in this ambient plasma. Hence, several physical mechanisms, which come into play at different instances, are involved. The combined effect of these mechanisms determines the penetration of the pellet, the rate at which it is ablated as well as the plasma density and temperature profiles after the injection. Moreover, the fuelling efficiency depends on these; hence a full understanding of all the involved mechanisms is mandatory.

2.1. Ablation and Homogenization models

As a cryogenic pellet traverses a magnetically confined plasma, it is ablated by interactions with background plasma particles (electrons, ions and impurities). However, it is also shielded from further direct interactions with ambient plasma by several mechanisms [3, 6, 7, 37, 38]. Subsequent to ablation, the ionized fraction of the ablatant expands along the magnetic field lines until plasmoid and plasma pressures balance, while also drifting down the magnetic field gradient. Plasmoid pressure relaxation with the background plasma determines the dynamics of the plasmoid and it is the driving term

for the **ExB** drift of plasmoid particles [13], which, for an arbitrary magnetic configuration, has the following form [19, 28, 29]:

$$\frac{dv_d}{dt} = -\frac{2(p_0 - p_\infty)\nabla_\perp B_\infty}{n_0 m_i B_\infty} \quad (1)$$

where p_0 and p_∞ are the pressure of the plasmoid and the background plasma (in units of Pa), respectively; $\mathbf{B}_\infty$ is the background magnetic field (in units of T), n_0 is the plasmoid density (in units of m^{-3}) and m_i is mass of plasmoid ions (in units of kg). Additionally, the change in the particle velocity distribution produced by plasmoid parallel expansion along a magnetic field line increases plasmoid acceleration [14]. On the other hand, Alfvén-wave emission from both ends of the cloud reduces the drift acceleration since it leads to losses of accumulated charges via parallel currents [19]. Moreover, two additional effects related to the short-circuiting of external and internal currents reduce the drift acceleration. The latter, Internal Circuit Closure, is produced by the short-circuiting of internal currents that arise to balance the variation of current accumulation on the plasmoid surface due to the rotation of magnetic field lines around the plasmoid center [15, 16]. The former, External Circuit Closure, consists of the depletion of accumulated charges when regions of opposite polarization become connected during the electric potential expansion [13]. Hence, all these effects modify the plasmoid drift, and, therefore, contribute to change the deposited material profile from the one that can be expected from the ablation profile.

2.2. HPI2 Code Description

The HIP2 code was developed to simulate the ablation of a cryogenic pellet (hydrogen, deuterium or a mixture of deuterium and tritium) injected into a magnetic confined plasma created in a tokamak device [10, 19] as well as the evolution of the pellet plasmoid, using a 0-D, two-cell, four-fluid Lagrangian system [13, 19, 39]. The code takes into account specific machine geometrical data, plasma energy and density profiles as well as the magnetic field configuration of the device. It should be noted that, although underlying ablation effects are machine independent, the calculation of the drift and the relative importance of the damping mechanism do depend on the device under consideration, particularly on whether the device is axisymmetric or not.

As mentioned previously, simulations with the HPI2 code were made for the LHD [29, 40], in which qualitative differences were found when compared with tokamaks. Therein, its extension to the complicated non-axisymmetric configurations required including the effect of a helical field in the calculation of the drift acceleration force [28, 29]. Furthermore, for the application of HPI2 to the W7-X and TJ-II scenarios, additional modifications are made to include a generalized calculation of the exact magnetic and geometric quantities, suitable for any tokamak or stellarator configuration, in the calculation of the drift; and to reduce the computation time. In this new stellarator version, the equilibrium magnetic configuration from the VMEC *wout*-file [41–43] is used to evaluate all drift-relevant magnetic and geometric quantities, averaged along plasmoid parallel lengths by employing a dedicated stellarator library. However, as will be outlined in section 4.1, target plasmas with low electron densities may be problematic, since pellet and plasma particle content can be similar. As a consequence, plasma cooling by the pellet

may be overestimated. In addition, since the magnetic field in stellarators depends strongly on toroidal position, ϕ, it varies along the plasmoid length. However, this variation is taken into account in a simplified manner when calculating the plasmoid drift, since only the averaged magnetic field along the plasmoid parallel length, <B>, acting at the plasmoid barycenter is considered. The fact that the three-dimensional variation of the magnetic field is not included in detail in the calculation of the plasmoid drift might be a limitation. However, it should be noted that, due to the finite rotational transform in a tokamak, the magnetic field strength also varies along the magnetic field line and thus along the plasmoid parallel direction (indeed, even for relatively small iota, due to the relative compactness, the variation of B on a flux surface is typically larger than in large-aspect ratio stellarators). Since HIP2 predictions have been validated for tokamaks [13, 20–23], this provides confidence for stellarators.

3. Device description

A number of pellet ablation and plasmoid drift experiments have been carried out in the stellarator TJ-II to clarify the influence of the fully three-dimensional magnetic field of non-axisymmetric devices on pellet fueling efficiency. Representative experimental results have been compared with simulations performed with the HPI2 code. In addition, the HPI2 code is used for pellet simulations in W7-X, which can be a support for the pellet injection plans in this recently commissioned device. In this section, both devices will be described. First, the characteristics of the TJ-II, together with its pellet injection system and relevant diagnostics, are reviewed. Next, the optimized stellarator W7-X is described along with a brief introduction about the pellet injection plans.

3.1. TJ-II

The TJ-II is a four-period, low magnetic shear ($\Delta\iota \leq 6$ %) stellarator located at CIEMAT, Madrid, Spain [44]. Its major radius, R_0, is 1.5 m, and its average minor radius, a_0, is $\leq$ 0.22 m. A set of poloidal, toroidal and vertical coils creates its fully 3-dimensional magnetic-field with bean shaped cross-section, central magnetic field, $B(0) \leq 1.1$ T, and total plasma volume of around 1.1 m^3. A wide range of vacuum magnetic configurations can be obtained, which allows exploring a broad variety of rotational transforms, $0.9 \leq \iota(0)/2\pi \leq 2.2$. Generally, hydrogen is used as the working gas. Plasmas, typically $\leq$ 300 ms, are created and maintained using ECRH and/or NBI. The two gyrotrons that form the ECRH system ($P_{ECRH} \leq$500 kW, $t_{discharge} \leq$300 ms) operate at 53.2 GHz, *i.e.*, the second harmonic electron cyclotron resonance frequency. The central electron densities, $n_e(0)$, and temperatures, $T_e(0)$, that can be achieved are $\leq 1.7\text{x}10^{19}$ m^{-3} (with particle content $\leq 1.9\text{x}10^{19}$, depending on magnetic configuration) and $\leq$2 keV, respectively. On the other hand, the NBI system is formed by two tangential injectors, one counter- and the other co-injected to the magnetic field direction, as seen in Figure 1 ($E_{NBI} \leq$32 keV, $P_{NBI} \leq$0.7 MW throughput). Central electron densities and temperatures of $n_e(0) \leq 5\text{x}10^{19}$ m^{-3} (particle content $\leq 5.5\text{x}10^{19}$) and $T_e(0) \leq$400 eV, respectively, can be achieved when a lithium coating is applied to the vacuum vessel wall [45]. The central ion temperature, $T_i(0)$, achieved with both heating schemes, is typically $\leq$120 eV. Under these conditions, good density control and plasma reproducibility are achieved, see [46]. An example of plasma evolution along a discharge is shown in Figure 2, where ECRH and co-NBI

heating are used. In this work, hydrogen pellets are injected into plasmas, using hydrogen as a working gas, created and/or maintained with ECRH and/or NBI.

3.1.1. Pellet injector and associated diagnostics

The TJ-II pellet injector (PI) is a four-barrel pipe gun device with a cryogenic refrigerator for *in-situ* cylindrical pellet formation (10 K), fast propellant valves for pellet acceleration (velocities between 800 m/s and 1200 m/s can be achieved) and straight delivery lines (see Figure 2). It was developed in collaboration with the Fusion Energy Division of Oak Ridge National Laboratory (ORNL), Tennessee, USA [33]. The TJ-II PI is a flexible system. Small pellets, type-1 (0.42 mm nominal diameter and length, and containing $\leq 4x10^{18}$ H atoms) and type-2 (0.66 mm nominal diameter and length, containing ≤ 1.2 $x10^{19}$ H atoms), are required to avoid raising the density above the gyrotron cut-off limit ($\sim 1.7x10^{19}$ m^{-3}). Larger pellets, type-3 (0.76 mm nominal diameter and length, and $\leq 1.8x10^{19}$ H atoms) and type-4 (1 mm nominal diameter and length, containing $\leq 4.1x10^{19}$ H atoms), are injected in high-density NBI-heated plasmas. The system has four injection lines, (labelled Line #1 to #4) with 54 mm separation between lines. The toroidal angle for Lines #1 and #2 is $\phi = 14°$, whereas it is $\phi = 13°$ for the other two (See Figure 3). Due to their position, only pellets injected from Lines #1 and #4 approach the plasma centre for standard configurations, whereas the flight paths for Lines #2 and #3 have nearest approach at $\rho = 0.273$ and $\rho = 0.45$, respectively, where $\rho = r/a$ is the normalized plasma radius. However, this is not a limitation, since pellet types can be interchanged between the four injection lines, so all pellet sizes can be injected into a path that crosses the magnetic axis [34]. Finally, good reproducibility of pellet mass and velocity is achieved. For instance, discharge #41777, simulated in Section 4, was part of a series of 8 injections of type-2 pellets (#41777 - #41787). Their mean pellet content and velocity were (6.3 ± 0.6) $x10^{18}$ H atoms and 838 ± 30 m/s, respectively. Similarly, of the 27 injections made in the series (#44607 - #44639), the mean pellet content and velocity were (6.3 ± 0.8) $x10^{18}$ H atoms and 900 ± 18 m/s, respectively. It should be noted that 5 of the latter pellets suffered friction losses or were broken upon plasma entry.

The PI is equipped with an in-line diagnostic system formed by a light gate and a microwave cavity. The signals from these systems are used to estimate the velocity and the mass of the pellet, respectively [33]. In addition, the light emitted by the neutral, or partially ionized, cloud that surrounds the pellet is collected by amplified silicon diodes and a fast-frame camera. Two amplified silicon photodiodes, fitted with interference filters centred at 660 (with full-width at half-maximum transmission of 10 nm) follow the Balmer H_α emission ($\lambda = 656.28$ nm) from above (TOP) and behind (SIDE) pellet flight paths (see Figure 2). The SIDE diode can be replaced by an avalanche photodiode. The pellet penetration depth and its ablation profile are determined, assuming that the pellet is not accelerated in the radial direction and that the H_α signal is proportional to the ablation rate. The time resolution of all the diode-based diagnostics is 1 μs. An ultra-fast CMOS camera, model FASTCAM APX-RS by Photron Incorp., San Diego, CA, normally records from a viewport located above the flight path (INNER TOP). It is equipped with coherent fibre bundle and machine-vision type camera lenses [47, 48]; in this work, a 12.5 mm lens, model HF12.5SA-1 by Fujinon Tokyo, Japan, has been used. The time resolution of the fast camera can be set, independently from the frame rate, from 1/frame rate to 1 μs in order to adapt to the experiment. On the other hand, the spatial

resolution varies from 1024 x 1024 pixels for full frame to 16 x 128 pixels at maximum frame rate (250 kfps), where each pixel corresponds to ~0.5 mm to ~1 mm along the pellet flight path, depending on the viewport used. The field-of-view of the system allows the plasmoid perpendicular to the pellet injection direction to be recorded, thereby permitting the study of pellet deflection and acceleration, both in radial and toroidal directions [49]. Apart from that, it is possible to record the trajectory of the pellet from a tangential, TANG, viewport, hence possible poloidal asymmetries and /or deflections can be determined, along with the plasmoid drift in both radial and poloidal directions. Moreover, it is possible to collect light from a rear viewport, SIDE. In this way, pellet poloidal deflection, plasmoid parallel expansion and poloidal drift can be study from a third line-of-sight (from behind the pellet injection path, as seen in Figure 1). However, since recording simultaneously from all viewports is not possible, the three-dimensional trajectory of the pellet cannot be determined, and some uncertainties may be present in the analysis.

3.1.2. Plasma diagnostics

TJ-II is equipped with a wide range of passive and active plasma diagnostics [50]. The diagnostics that are relevant for pellet injection studies include the Thomson Scattering (TS) system, which provides one set of electron density and temperature profiles, with 160 spatial positions (~2 mm spatial resolution), per discharge [51]; a microwave interferometer, with 10 μs of time resolution, that follows the line-integrated electron density along the discharge, and an eleven-channel Electron Cyclotron Emission (ECE) system that follows the electron temperature evolution at different radii. The positions of these diagnostics, relative to the PI location, are shown in Figure 1. Due to the limited number of measurements per discharge of some of the diagnostics (e.g. TS has 1 per discharge), the shot-to-shot technique is frequently employed, i.e. pellets are injected into reproducible plasmas and a single measurement per discharge is made at a different time for every shot.

3.2. Wendelstein 7-X

The Wendelstein 7-X is an optimized stellarator that was commissioned at the end of 2015 [52]. The first, and limited, phase of operation of this large device was completed in early-2016 [53]. Its main goal is to achieve steady-state operation at high normalized pressure with a volume-averaged beta, β, of about 5 %, ion temperatures of several keV and plasma densities higher than 10^{20} m^{-3}, and, hence demonstrate the viability of the stellarator as a fusion reactor. It is expected that its optimized magnetic field configuration will enable significantly better plasma performance respect to non-optimized magnetic field geometries [36, 54, 55]. This optimized magnetic field is generated by a set of 70 superconducting NbTi coils. From these, 50 non-planar modular coils provide the basic rotational transform, while 20 planar coils allow varying the rotational transform and adjusting the radial position of the plasma. In addition, 10 non-cryogenic conducting coils enable sweeping of the divertor strike lines while 5 additional coils are used for plasma edge control and error field correction. This set of coils makes achieving a maximum magnetic field of 3 T possible.

The W7-X major radius is R = 5.5 m, while its average minor radius is $\langle a \rangle$ = 0.55 m; this corresponds to a plasma volume of about 30 m^3. Its main steady-state heating

system is an ECRH system [32, 56] formed by 10 gyrotrons, with output power of 1 MW per gyrotron, operating at 140 GHz, the 2nd harmonic of the electron cyclotron resonance at 2.5 T. It is planned to use the 2nd harmonic X-mode (X2) for plasma start-up and at low plasma electron densities, whereas, it is expected to change to the 2nd harmonic O-mode (O2) for densities above the X2 cut-off density (1.2×10^{20} m^{-3}). In addition, two NBI, with maximum pulse length, $t_{discharge} \leq 10$ s, will provide $P_{NBI} = 1.7$ MW of neutral power per injector by the injection of neutral hydrogen atoms accelerated to 55 keV; deuterium injection will also be possible ($P_{NBI} = 2.5$ MW, 60 keV) [57]. Moreover, an Ion Cyclotron Resonance Heating system will provide heating to complement the ECRH system [58]. During the first part of the first phase of its operation, OP1.1, pellet injections were not available on the W7-X [59]. Nonetheless, a recommissioned blower-type injector [60] is to be employed during the OP 1.2 phase while a new extrusion type injector will be available at a later date.

3.2.1. W7-X pellet injector

The ASDEX Upgrade blower-gun injector [60] is currently installed on W7-X. This has been done in order to determine if injection location is critical for achieving efficient core fueling, as in tokamaks, and if the beneficial inwards drift is present in W7-X for HFS injection, unlike in LHD. Injections of cylindrical hydrogen pellets, 2 mm in diameter and 2 mm in length (containing 3.3×10^{20} H atoms), are planned for the OP1.2 operational phase. These pellets will be accelerated to speeds of around 250 m/s and injected into W7-X from two different injections ports, one located in the HFS part (AEL41) of the vessel and the other on the LFS (AEK41). Since these two ports, see Figure 4 a) and b) (the use of Figure 4 c) is clarified later) are toroidally close ($\phi_{HFS} = -2.22$ rad, $\phi_{LFS} = -2.24$ rad) comparison studies can be undertaken.

4. Pellet ablation (experiments and predictions)

Hydrogen pellet injection experiments have been performed in on/off- axis ECRH and NBI hydrogen plasmas, with different densities, created using the TJ-II standard configuration, called 100-44-64 (the numbers refer to currents in the central, helical and vertical coils, respectively) (see Figure 3 and Figure 5). Pellet ablation profiles are determined from the recorded Balmer H_α emission, assuming that this emission provides a reasonable indication of the ablation rate and the penetration depth [61]. In addition, in-line light-gate and microwave cavity signals are used to establish the timing and pellet mass. It is also assumed that the pellet is not radially accelerated while it crosses the plasma. Fast-camera images are used to verify that the radial acceleration of the pellet is indeed negligible. This can be determined from Figure 6, where a montage of snap-shot series of pellet images, corresponding to discharge #44624 is shown. Here, a type-2 pellet is injected along Line #1 into a standard-configuration ECRH plasma. From this, nearly constant radial separations are found between the emission maximum of each image, Figure 7, which signifies that the radial velocity is constant along the pellet trajectory. Hence, the assumption of constant radial velocity is justified (from geometrical considerations for INNER TOP, 1 pixel ≈ 0.52 mm for upper injection lines (Line #1 and #4) and 1 pixel ≈ 0.56 mm for Line #2 and #3).

Representative montages of snap-shot images, recorded from above (INNER TOP), for individual pellets injected into standard configuration ECRH and NBI plasmas

are shown in Figure 8 a) and Figure 9 a), along with the H_α emission detected by the photodiodes (see Figure 8 b) and Figure 9 b)). Next, representative images recorded from the tangential (TANG) viewport, along with the H_α emission, are shown in Figure 10 and Figure 11 for individual pellets injected into ECRH (Pellet-2 in Line # 1) and NBI (Pellet-3 in Line #4), respectively, heated plasmas. It should be noted here that the x-axis in Figure 6, and Figure 8 to Figure 11 is directed along the device major radius, while the y-axis corresponds to the toroidal direction. It can be seen in Figure 8 a) and Figure 10 a) that the pellet trajectory for ECRH plasmas is not deviated, rather it continues along the original pellet injection line until fully ablated. However, for plasmas maintained with unbalanced NBI heating, the pellet is deflected, in both toroidal (see Figure 9) and poloidal (Figure 11) directions. Cloud asymmetries are not detected for pellets injected into either ECRH or NBI plasmas [49]; for pellets injected into ECRH plasmas, this is consistent with the fact that pellet trajectory is not deviated from the original injection path. On the contrary, pellets injected into unbalance NBI plasmas are deviated without any observed cloud asymmetry. Such deflections are usually related to an ablation asymmetry [40]. However, for the TJ-II case, calculations indicate that a heating asymmetry alone cannot explain the trajectory deviation, rather, they can be associated to momentum transfer from NBI fast ions or a combination of both [49]. Unfortunately, the current fast-camera system does not allow determination of the actual acceleration direction. Toroidal accelerations of the pellet of the order of $10^3 – 10^4$ km/s have been reported [49] for both co- (NBI 1) and counter- (NBI 2) injections. However, the observed poloidal accelerations are different for both type of injections; negligible poloidal accelerations are estimated for NBI 1 comparing to toroidal accelerations (of the order of 10 km/s), while poloidal accelerations observed for NBI 2 are of same order than radial accelerations, 10^3 km/s). Additionally, the direction of the magnetic field lines can be observed in the fast-camera images, since the partially ionized part of the cloud expands along these. It is also observed in Figure 9b) that, when the pellet crosses the magnetic axis, i.e., it crosses an already cooled region, the amplitude and frequency of the striations appear to reduce. Additional examples of H_α profiles corresponding to pellets that penetrate beyond the magnetic axis can be found in refs. [34, 47].

The expected outwards-directed drift of the ablated material in TJ-II [34] is observed in fast-camera images (see Figure 12); it is also possible to determine the drift velocity of the plasmoid in the radial and poloidal directions from these images. First, using images from the INNER TOP camera viewport, the magnitude of the radial drift is estimated. The radial asymmetry observed in the light profile of each snap-shot image (see Figure 6) can be attributed to such a radial, outward-directed drift. To estimate the magnitude of this radial drift velocity, each light profile is fitted with two Gaussian curves; the main one represents the ablating pellet, whereas the second one represents the drifting plasmoid. From the differences between the radial positions of such peaks and the exposure time ($\tau_{exp} \sim 4$ μs), values between 2 and 5 ± 0.003 km/s are obtained for the average drift velocity in ECRH plasmas, which are inside the expected range [62]. An equivalent analysis is carried out for tangential images, where both the drift in the poloidal direction and in the radial direction can be estimated. A representative snapshot image from #45110 (pellet-3 injected along Line #4 into almost balance NBI phase) is shown in Figure 12, where the direction of the drift is highlighted; it is observed here that the plasmoid drifts towards the LFS plasma edge and towards the plasma bottom. For ECRH

plasmas, average drift velocities in the radial direction between 6.5 ± 0.7 km/s and 7 ± 0.7 km/s are found ($\tau_{exp} \sim 4$ μs); while for the drift velocities in the poloidal direction, the values obtained are between 2.5 ± 0.7 km/s and 5.6 ± 0.7 km/s. On the other hand, for pellets injected into NBI plasmas, average drift velocities in the radial direction of between 4 ± 5 km/s and 12 ± 5 km/s are obtained for an exposure time, τ_{exp}, of 2 μs, while velocities of 1.4 ± 3 km/s to 10 ± 3 km/s are obtained for $\tau_{exp} \sim 4$ μs. In contrast, for drift in the poloidal direction, the average velocities are found to be between 5 ± 6 km/s and 10 ± 6 km/s for the short exposure time and between 1.5 ± 3 km /s and 7.6 ± 3 km /s for the long one. The differences in the uncertainties between ECRH and NBI cases are explained by considering that pellets injected into NBI plasmas are deflected and, hence, the light emitted as the pellet changes its direction, both toroidally and poloidally, is superimposed onto the radial and poloidal drifts, blurring the images and increasing the incertitude in the estimation of the drift. The reason for differences related to the exposure time will be discussed later. In addition, smaller uncertainties are achieved for radial drift velocities deduced from INNER TOP port images than for TANG. This is due to the calculation procedure of the camera-to-pellet-path distance, which is directly obtained for the INNER TOP viewport; in contrast to TANG port, which requires a more elaborate calculation, and hence, uncertainties are increased. It should be noted however that it is not possible to determine poloidal drift displacements from INNER TOP images. Although the pixel size to pellet path distance ratio is constant along the pellet path, it changes with focal length, *i.e.*, the plasmoid drifts downwards and the pixel-distance ratio changes. Therefore, the radial drift velocity is underestimated, so inclusion of this incertitude yields an uncertainty of ± 0.7 km/s.

Since pellet velocity is known and there is no acceleration, the temporal evolution of the H_α emission can be transformed into a radial emission profile, and, compared with the time-integrated light profile of the images recorded with the fast camera (possible errors may come from neglected poloidal deflection in the case of upper view, and toroidal for the tangential view, since the fast-camera system does not allow studying the 3D trajectory of the pellet). Such profiles are shown in Figure 8b) to Figure 11b) for TJ-II discharges #44828, #41391, #45110 and #45091, respectively. Good agreement is found between the spatially resolved profile from the fast camera and the temporal evolution of the H_α emission when constant velocity is assumed, even though some differences are present. For instance, fast camera lens is not equipped with a filter, hence all the visible light emitted by the shielding cloud is recorded. Moreover, the fact that the plasmoid is drifting backwards is not taken into account in the transformation of the temporal evolution of the H_α emission into spatial coordinates. In addition, it should be also considered that the fast camera image may be saturated (see, for instance, Figure 11b)). Hence, it is confirmed that the supposition of no radial acceleration is reasonable.

4.1. Modelling of pellet injections and comparison with TJ-II experiments

Hydrogen pellets of different sizes have been injected into both ECR- and NBI-heated plasmas having a range of plasma densities and temperatures. The previously mentioned HPI2 code is used to simulate pellet injection into ECRH TJ-II plasmas in the standard configuration. The ablation and deposition profiles, as well as the temperature evolution, obtained with this code are compared with the measured H_α emission; and with density and temperature profiles acquired with the Thomson Scattering system (TS). It should be

noted that the peak observed close to the edge of the TS target temperature profile (at ρ = 0.75) is also observed in the H_α profile. Therefore, it may not be an artefact of the diagnostic, but real, possibly related to a rational surface at that radial position [63]. In Figure 13, ablation profiles calculated by the HPI2 code are compared with H_α emissions detected by TOP photodiode. In Figure 13a) and b), plasma discharge #41777 (target plasma: $n_e(0) = 6x10^{18}$ m^{-3}, $T_e(0) = 1.1$ keV), into which a pellet type-2, containing $6.1x10^{18}$ H^0, was injected at 808 m/s into an off-axis ECRH plasma, through Line #1, is shown. The agreement between the recorded H_α, which gives an indication of the ablation rate, and the predicted ablation profile is reasonably good, considering that the H_α emission is not directly proportional to the ablation rate. It should be noted that off-axis ECRH generates a suprathermal electron population within the plasma core that enhances ablation at the end of the pellet lifetime [64]. Its presence is identified by hard X-ray emission along the whole plasma discharge, as can be observed in Figure 14, this being due to deconfined suprathermal electrons interacting with the vacuum chamber wall. However, the overall effect of suprathermal electrons on the ablation rate is reduced, since the population encountered by the pellet as it crosses the plasma is very small, and the main suprathermal population is located near the plasma centre, where it is almost completely consumed. The effect of such fast electrons in pellet ablation is not included in this version of the code. A second example, corresponding to #44614 (target plasma: $n_e(0) = 8.2x10^{18}$ m^{-3}, $T_e(0) = 1.87$ keV) is found in Figure 13c) and d). Here, a pellet type-2, containing $6.6x10^{18}$ H^0, was also injected thought Line #1 at 900 m/s into an on-axis ECRH plasma. In this case, a relatively strong peak is observed in the H_α emission before ablation is completed. However, it is considered that not all recorded light is directly related to pellet ablation. For instance, it can be deduced from fast camera images that the photodiodes are also sensitive to emissions from drifting plasmoids. In addition, it can be seen in Figure 14 that pellet injection triggers a brief emission of hard X-rays, considered to be due to the deconfinement of suprathermal electrons located near low-order rational surfaces. These fast electrons do not seem to have any effect on the ablation rate, as observed in Figure 13 c) for the comparison between the predicted ablation profile and the light profile obtained from the montage of snap-shot fast camera images. The penetration depth, *i.e.* distance travelled by the pellet until its complete ablation, of the pellet is well predicted by the HPI2 code, as well as the rate of the ablation, whose shape is similar to the H_α emission, considering the expected differences.

The density profiles of these plasmas, after the complete ablation of the pellet and homogenization of the ablated material, predicted by the HPI2 code are shown in Figure 15, together with those of the target plasmas, measured by the TS. In addition, densities measured by the TS at different times after the injection of a pellet, for reproducible discharges, are plotted, so the time evolution of the plasma density can be reconstructed [34]. Moreover, the evolution of the deposition profile, *i.e.*, the increment of the plasma density, can be observed in this figure. The use of the shot-to-shot technique to reconstruct post-injection density and temperature, and deposition profiles (see Figure 15 to Figure 17) is justified by good plasma and pellet reproducibility. For instance, for the discharge series (#41777 - #41787), the target line-averaged densities were 5.2 ± 0.2 x 10^{18} m^{-3} [34], albeit for simulation the chosen discharges had a smaller difference (≤ 0.1 x 10^{18} m^{-3}). While for series (#44607 - #44639), the target line-averaged densities were 4.9 ± 0.1 x 10^{18} m^{-3}. In Figure 15 a) results corresponding to discharge #41777 are shown; while in

Figure 15 b), results for #44614 are plotted. It can be observed in both cases that the plasma density given by the HPI2 code is shifted towards outer radii, compared to the experimental profiles. However, it should be noted that the code does not take into account particle transport, so the density profile, at the injection toroidal position (ϕ = 14º), is calculated when the homogenization of the material is completed (in these particular cases, ~0.32 ms and ~0.3 ms, respectively, after the injection of the pellet); in contrast, TS measurements are made at ~0.8 – ~1 ms after pellet injection, since, from experimental observations, it is established that this is the time required to achieve complete particle distribution [34], and hence, no clear change is observed before that time in TS profiles. Therefore, it is necessary to simulate the time evolution of this density profile, considering transport, to accurately compare the simulation result with the measured ones. The density profile at time t = +0.8 ms for #41777 (t = +1.48 ms for #44614) after the injection of the pellet is calculated using neoclassical simulations with DKES [42] as explained in detail in [35] and the result is also plotted in Figure 15. Neoclassical transport is considered here as it has been shown to reproduce the transport of ablated material towards the plasma core [35]. Generally speaking, it is seen that the pellet injection creates density profiles that are more hollow than before. If this is the main change in the shape of the plasma profiles in the particle time scale (the electron temperature goes back to previous values on a faster time scale), neoclassical transport should lead to an increase of the core density, as discussed in [35] for TJ-II NBI plasmas. Together with this, there should be a drop of the density in the outer regions and a transiently constant density at intermediate radial positions. This goes qualitatively in the right direction, and indeed the density profiles calculated including neoclassical transport are closer to the corresponding Thomson Scattering profiles than those estimated by HIP2 only. However, the quantitative agreement can be considered reasonably good for discharge #44614 but poorer for discharge #41777. Moreover, despite the overall good agreement of discharge #44614, the neoclassical simulation predicts a density lower than the target density, around ρ ~0.15, which is not observed in the experiment and it is as odds with the general description given above. It is first noted that the radial electric field also evolves after pellet injection within the time scale of particle transport [35], as does the ambipolar radial electric field in these simulations. It is also noted that in discharge #44614 the core electron temperature is relatively high, which means that the radial electric field (approximately given by $\frac{1}{e}\frac{dT_e}{dr}$) is large and DKES simulations become inaccurate [65]. In addition, regarding discharge #41777, it should be recalled that the presence of suprathermal electrons is not considered in the calculations. The presence of such a population may explain the disagreement between measured and predicted density profiles. Finally, changes in the particle sources from the wall are neglected in transport simulations. However, there is no indication that part of the pellet fuel goes to the wall, even though the estimated fuelling efficiency is low [34]. In contrast, the efficiency estimated from HPI2 simulations is high, at ~80% for the cases considered here. When neoclassical transport is considered, the fuelling efficiency is considerably reduced. Values are estimated to lie between 60-70% for #41777 and 30-50% for #44614, these being significantly higher than the experimental ones (~25% for both cases). In order to account for this, it is considered that the number of particles deposited near the plasma edge may be overestimated due to a numerical artefact that appears when drift displacement is large, with the result that a substantial and unknown fraction of particles

is not considered lost. In addition, it is not possible to determine accurately the density evolution with DKES for radial positions outside $\rho \geq 0.8$. Therefore, such uncertainties in the estimation of fuelling efficiency are important, and hence, may explain the differences with experimental values.

Simulated electron and ion temperature profiles for 0.3 ms after pellet injection, i.e. HPI2 post-injection temperature profiles, are plotted in Figure 16 and Figure 17 for #41777 and #44614, respectively. In the same figures, temperature profiles, measured by the TS system, before and at 0.8 ms and 1.48 ms after pellet arrival at the plasma edge respectively, are also shown. Since plasma cooling and recovery during and after pellet ablation are faster than plasma density changes, it is difficult to determine from TS profiles whether this cooling effect is overestimated by HPI2 calculations. However, in ref. [34], it is shown that processes associated with pellet ablation are mainly adiabatic, which concurs with assumptions made for HPI2.

In addition to the above, the magnitude of the drift velocity is predicted by the HPI2 code; for #41777, drift velocities between 0.6 km/s and 3.8 km/s are found, when the plasmoid is detached from the pellet, whereas, when the plasmoid is completely ionized, the obtained values are between 1.4 km/s and 3.8 km/s. In addition, during the homogenization phase, radial drift velocities up to 2.5 km/s to 20 km/s are reached, while poloidal drift velocities of between 1 km/s and 10 km/s are attained. Similarly, for #44614, the magnitude of the drift velocity predicted are between 0.4 km/s and 5.1 km/s (for the detached plasmoid), and between 0.9 km/s and 5.1 km/s (for the completely ionized plasmoid). Also, during the homogenization phase, the maximum velocities obtained are between 1.4 km/s and 23 km/s for the radial direction and between 0.7 km/s and 14 km/s for the poloidal direction. Moreover, the time evolution of a single plasmoid drift velocity from $\rho \sim 0.8$, for both cases, is shown in Figure 18, where both radial and poloidal components are plotted; here, it is observed that the drift velocity is initially accelerated (until $t \sim 35\ \mu s$), and after that, it is decelerated until the motion is completely stopped. The initial acceleration and subsequent deceleration concur with the fact that the estimated average drift from fast camera images depends on exposure time. Furthermore, the values of the drift velocities, in both the radial and the poloidal direction, calculated with the HPI2 code agree reasonably well with the averaged values estimated from fast camera images. On the other hand, the direction of the drift is given by the magnetic field, in particular by the inverse curvature radius, and since TJ-II is a fully 3D device, this depends on the parallel length of the plasmoid. So, in HPI2, as mentioned in the description of the code, the inverse curvature radius is averaged along the whole plasmoid length and, this average value is used to calculate the effective drift of the plasmoid.

Examples of the inverse curvature radius vector field are plotted in Figure 19 and Figure 20 for plasmoids whose dimension parallel to the magnetic field lines, Z_0, is 0.8 m and 10 m, where it can be seen that the drift is directed radially outwards and poloidally downwards for plasmoids of short parallel length and, as they expand, the drift becomes inwards-directed. In addition, the complete trajectory of each plasmoid during the homogenization phase for #41777 is plotted in the same figures, so it can be seen that plasmoids drift following the direction of the inverse curvature radius at the corresponding parallel length. It is also observed that most plasmoids drift to the plasma edge and are partially or completely lost, while only some of them are stopped before

reaching the edge, explaining the density profile shifted to the LFS plasma edge with respect to the ablation profile, and the low fuelling efficiency of pellet injections in this type of plasmas, where pellets do not penetrate to beyond the plasma centre [34]. Finally, it should be noted that a detailed comparison with experimental results is not possible with the current fast camera system, since, in addition to time average effects, due to finite exposure time, fast camera images are only able to show the drift of the plasmoid at the beginning of the homogenization phase, when the parallel length of plasmoid is short compared to the length of the field line, referred as self-connection length [13], i.e. when no average effect has come into play yet. It is found that the direction given by the HPI2 code for plasmoids of small parallel length, agrees with the drift estimated from fast camera images (see Figure 12) and with the deposition profiles shifted towards the LFS plasma edge, an effect that has been reported for LFS injections in several tokamaks [5], [13, 62] and in the LHD [66].

4.2. Simulation of pellet injections for Wendelstein 7–X

A preliminary comparison of pellet penetration and material deposition for LFS and HFS injections has been performed using the new version of the HPI2 code to simulate the injection of hydrogen pellets into W7-X from the two ports, indicated in section 3.2.1. In the simulations, possible erosion of the pellet due to friction off the inner guide tube walls is considered by using a smaller pellet diameter (d_p = 1.5 mm). Hence, the number of hydrogen atoms in such a pellet is 1.9×10^{20}, compared to 3.3×10^{20} for a 2-mm pellet. Moreover, these simulations are performed for two different plasma scenarios; the high temperature case corresponds to ECR heating in X2-mode, whereas the second one, the high-density case, corresponds to ECRH in O2-mode. Hence, the impact of background plasma is also evaluated. The density and temperatures profiles of both plasma scenarios are plotted in Figure 21. Ablation and deposition profiles of the four different cases are plotted in Figure 22, while penetration depth and fuelling efficiency are found in Table 1. The HPI2 code predicts that pellet injection into W7-X plasmas from the HFS allows the ablated material to achieve deeper deposition and higher efficiency, as seen in Figure 22 and Table 1. Furthermore, a slightly deeper deposition is expected for injections into high temperate plasmas (ECRH in X2-mode) since a larger difference between plasma and plasmoid density, due to larger ablation rate, enhances the drift (see equation 1). On the other hand, for LFS-injection, deeper deposition should be achieved for high-density plasmas (ECRH O2-mode), since the lower temperature of O2-mode plasmas increases pellet penetration and the larger density difference in the X2-mode ECRH enhances the outward-directed drift of material.

In addition, two LFS injection ports, indicated in Figure 4 b) and c), are compared as a preliminary study for the design of a new pellet injection system. For that, simulations of two different pellet sizes are carried out, varying the velocity of the pellet from 200 m/s to 1000 m/s and for the same plasma scenarios. An example of ablation and deposition profiles obtained for 3 mm long and 2.8 mm diameter pellets (containing 8.9×10^{20} H atoms) at 600 m/s is shown in Figure 23, while the fuelling efficiency for all the different cases is plotted in Figure 24. According to the results of the simulations, it is possible to determine that, even though the penetration of the material is similar for both injection ports, AEK41 is the most suitable, since fuelling efficiency is higher, particularly for large and fast pellets (see Figure 24), due to differences of the inverse

curvature radius. As can be seen in Figure 25, the inverse curvature radius in the toroidal position corresponding to AEE41 port is significantly larger for plasmoids of short parallel length, comparing with the plasmoid self-connection length; for larger plasmoids, average effects remove this difference.

5. Conclusions

Pellet of different sizes have been injected into TJ-II plasmas. H_α emission detected by photodiodes, and fast camera images have been used to study the ablation, along with the drift velocity and direction for several plasma characteristics. In addition, TS measurements have been employed to analyse the time evolution of the plasma density profile, and to study the relation between the estimated drift and the shape of the deposition profiles. From these, first, the assumption of non-radial pellet acceleration is confirmed using a fast-frame camera. In addition, fast-frame snap-shot images are used to estimate the time average drift velocity. The radial component is found to be 1.4 -12 km/s, depending on the heating method and the exposure time; while time-average poloidal drift is estimated to be of between 1.5 km/s and 10 km/s. Second, under the assumption of constant radial pellet velocity, the temporal evolution of the H_α emission is transformed into a radial profile and compared with the ablation profile obtained with the HPI2 code for injections into ECRH plasmas. The agreement is found to be acceptable, considering that the measured H_α emission is only an indication of the ablation rate and not proportional to it. Moreover, the agreement improves significantly when average-H_α emission profiles are considered. Also, for #44614, for which the fast camera was available, the comparison between predicted ablation and light emission profiles is considerably better. In addition, when deposition profiles reconstructed from shot-to-shot TS measurements, are compared with simulation results, it is seen that simulated profiles are shifted towards the LFS plasma edge with respect to the experimental ones. However, due to the time delay between TS measurements and pellet injection time, it is necessary to consider neoclassical transport. For this, the HPI2 density profile temporal evolution is followed using the DKES code. Even though the agreement between ablation profiles and simulated ones is satisfactory for both cases, the TS post-injection density profile is reasonably reproduced only for #44614. The experimental post-injection density of #41777 cannot be reproduced by simulations, although the result shows the right tendency, i.e. increment of the core density and reduction of the edge density. Such disagreement is mainly related to the presence of suprathermal electrons, whose associated effects are not included in this version of the HPI2 code.

Next, simulations were carried out for hydrogen pellets injected into W7-X plasmas. Since the agreement between TJ-II experimental and simulated results is considered to be acceptable for on-axis ECRH plasmas, the predictions made for W7-X should be reliable, providing the population of suprathermal electrons is not significant. Therefore, in such cases, higher efficiency of the fuelling and deeper penetration of the ablated material are expected for HFS injections, due to the inwards-directed drift experienced by plasmoids detached in the inner part of the plasma. In particular, injections into high-temperature plasmas are expected to be especially advantageous, since the larger difference between plasma and plasmoid pressures enhances the drift. Regarding the preliminary study for the design of a new pellet injector for W7-X, one injection port – AEK41 – is identified as the most suitable since fuelling efficiency is higher due to the

smaller inverse curvature radius, which does not have an associated outwards drift as large as the AEE41 port.

In the future, further experimental studies are intended to be carried in TJ-II; for instance, a scan of iota profile and magnetic well, which may lead to a deeper understanding of the influence of the magnetic field and the reconnection length in the deposition of the ablated material and the efficiency of the fuelling in stellarators, taking advantage of the ability of TJ-II to operate in a broad range of magnetic configurations. These experimental studies can be complemented with simulations employing the HPI2 code. In addition, images of pellets injected into co- and counter-NBI plasmas can be used to confirm whether the neutral beam injections are balanced enough to avoid the toroidal deflection caused by unbalance injection, and, if they are indeed balance, the effect of fast ions in the ablation could be simulated with this version of the HPI2 code. Moreover, it is considered essential to include the effect of suprathermal electrons in order to determine whether their presence can explain the observed discrepancy between predicted density profiles and TS measurements, particularly for off-axis ECRH plasmas. Furthermore, optimization of the fast camera system could lead to improve estimations of the drift velocity; it can also be modified to follow the injection from behind the pellet. These modifications of the fast camera system may facilitate the comparison of experimental results and predictions and, therefore, complete the benchmarking of the HPI2 code for W7-X.

Acknowledgments

This work has been carried out within the framework of the EUROfusion Consortium and has received funding from the Euratom research and training programme 2014-2018 under grant agreement No 633053. The views and opinions expressed herein do not necessarily reflect those of the European Commission. In addition, it is partially financed by grants from the Spanish Ministerio de Economía y Competitividad (Refs. ENE2013-48679-R and ENE2015-70142-P). The authors thank the TJ-II team for their assistance with the work.

References

[1] H. Maaßberg *et al.*, "Transport in stellarators," *Plasma Phys. Control. Fusion*, vol. 35, pp. B319–B332, 1993.

[2] M. R. Mikkelsen *et al.*, "Core fuelling to produce peaked density profiles in large tokamaks," *Nucl. Fusion*, vol. 35, no. 5, pp. 521–533, 1995.

[3] B. Pégourié, "Review: Pellet injection experiments and modelling," *Plasma Phys. Control. Fusion*, vol. 49, no. 8, p. R87, 2007.

[4] L. R. Baylor *et al.*, "Pellet fuelling deposition measurements on Jet and TFTR," *Nucl. Fusion*, vol. 32, no. 12, pp. 2177–2187, 1992.

[5] P. B. Parks, W. D. Sessions, and L. R. Baylor, "Radial displacement of pellet ablation material in tokamaks due to the grad-B effect," *Phys. Plasmas*, vol. 7, no. 5, pp. 1968–1975, 2000.

[6] P. B. Parks, R. J. Turnbull, and C. A. Foster, "A model for the ablation rate of a solid hydrogen pellet in a plasma," *Nucl. Fusion*, vol. 17, no. 3, pp. 539–

556, 1977.

[7] W. A. Houlberg, S. L. Milora, and S. E. Attenberger, “Neutral and plasma shielding model,” *Nucl. Fusion*, vol. 28, no. 4, pp. 595–610, 1988.

[8] L. R. Baylor *et al.*, “An international pellet ablation database,” *Nucl. Fusion*, vol. 37, no. 4, pp. 445–450, 1997.

[9] W. A. Houlberg *et al.*, “Pellet penetration experiments on JET,” *Nucl. Fusion*, vol. 32, no. 11, pp. 1951–1965, 1992.

[10] B. Pégourié *et al.*, “Modelling of pellet ablation in additionally heated plasmas,” *Plasma Phys. Control. Fusion*, vol. 47, no. 1, pp. 17–35, 2005.

[11] R. Samulyak, T. Lu, and P. Parks, “A magnetohydrodynamic simulation of pellet ablation in the electrostatic approximation,” *Nucl. Fusion*, vol. 47, pp. 103–118, 2007.

[12] P. B. Parks, T. Lu, and R. Samulyak, “Charging and rotation of ablation clouds surrounding refueling pellets in hot fusion plasmas,” *Phys. Plasmas Phys. Plasmas Phys. Fluids*, vol. 16, no. 21, p. 60705, 2009.

[13] B. Pegourie, V. Waller, H. Nehme, L. Garzotti, and A. Geraud, “Homogenization of the pellet ablated material in tokamaks taking into account the ∇B-induced drift,” *Nucl. Fusion*, vol. 47, no. 1, pp. 44–56, 2007.

[14] P. B. Parks and L. R. Baylor, “Effect of parallel flows and toroidicity on cross-field transport of pellet ablation matter in tokamak plasmas,” *Phys. Rev. Lett.*, vol. 94, no. 12, pp. 1–4, 2005.

[15] V. Rozhansky, I. Senichenkov, I. Veselova, and R. Schneider, “Mass deposition after pellet injection into a tokamak,” *Plasma Phys. Control. Fusion*, vol. 46, no. 4, pp. 575–591, 2004.

[16] I. Y. Senichenkov, I. Y. Veselova, V. A. Rozhansky, and R. Schneider, “Modeling of the pellet cloud structure in the presence of ∇ B induced drift,” *J. Nucl. Mater.*, vol. 337–339, no. 1–3 SPEC. ISS., pp. 446–450, 2005.

[17] N. Commaux *et al.*, “Influence of the low order rational q surfaces on the pellet deposition profile,” *Nucl. Fusion*, vol. 50, no. 2, p. 25011, 2010.

[18] R. Sakamoto *et al.*, “Cross-field dynamics of the homogenization of the pellet deposited material in Tore Supra,” *Nucl. Fusion*, vol. 53, no. 6, p. 63007, 2013.

[19] F. Koechl *et al.*, “Modelling of Pellet Particle Ablation and Deposition : The Hydrogen Pellet Injection code HPI2,” *Prepr. EFDA–JET–PR(12)57*, p. 82.

[20] D. Frigione *et al.*, “Particle deposition, transport and fuelling in pellet injection experiments at JET,” *Prepr. EFDA–JET–CP(10)08/48 D*.

[21] F. Koechl *et al.*, “Integrated Modelling of Pellet Experiments at JET,” in *Plasma Physics (Proc. 37th EPS Conf. Dublin, 2010)*, 2010, vol. 34A, p.

O4.123.

[22] L. Garzotti *et al.*, “Pellet fuelling physics studies on MAST,” in *41st EPS Conference on Plasma Physics ECA Vol. 38F*, 2014, pp. 2–5.

[23] P. Klaywittaphat, T. Onjun, and R. Picha, “Effect of magnetic field on pellet penetration and deposition in ohmic Tore Supra discharges.,” in *38th EPS Conference on Plasma Physics ECA Vol. 35G*, 2011, p. P4.135.

[24] Y. S. Na *et al.*, “On Benchmarking of Particle Transport Simulations in ITER,” *EUROFUSION WPJET1-CP(16) 15339*, p. 8.

[25] L. Garzotti *et al.*, “Simulations of density profiles, pellet fuelling and density control in ITER,” *Nucl. Fusion*, vol. 52, no. 1, p. 13002, 2011.

[26] B. Pégourié, C. Day, A. Frattolillo, F. Koechl, and P. T. Lang, “Physical constraints on the design of the DEMO pellet fueling system,” in *ECA Vol. 40A*, 2016, vol. 97, pp. 3–6.

[27] P. Vincenzi *et al.*, “Fuelling and density control for DEMO,” *Nucl. Fusion*, vol. 55, no. 11, p. 113028 (11pp), 2015.

[28] A. Matsuyama, F. Koechl, B. Pégourié, R. Sakamoto, G. Motojima, and H. Yamada, “Modeling of drift displacement of the pellet ablated material for outboard side injection in large helical device,” *Plasma Fusion Res.*, vol. 7, no. 2012, pp. 1–5, 2012.

[29] A. Matsuyama, F. Koechl, B. Pégourié, R. Sakamoto, G. Motojima, and H. Yamada, “Modelling of the pellet deposition profile and ∇B -induced drift displacement in non-axisymmetric configurations,” *Nucl. Fusion*, vol. 52, no. 12, p. 123017, 2012.

[30] H. Yamada *et al.*, “Configuration flexibility and extended regimes in Large Helical Device,” *Plasma Phys. Control. Fusion*, vol. 43, pp. A55–A71, 2001.

[31] R. Sakamoto *et al.*, “Ablation and Subsequent Density Redistribution of Fueling Pellets Injected into LHD Plasmas,” *EPS poster*, vol. 26, no. June, p. 2002, 2002.

[32] J. Geiger *et al.*, “Aspects of steady-state operation of the Wendelstein 7-X stellarator,” *Plasma Phys. Control. Fusion*, vol. 55, no. 1, p. 14006, 2013.

[33] S. K. Combs *et al.*, “Results from Laboratory Testing of a New Four-Barrel Pellet Injector for the TJ-II Stellarator,” *Fusion Sci. Technol.*, vol. 64, no. 3, pp. 513–520, 2013.

[34] K. J. McCarthy *et al.*, “Plasma fuelling with cryogenic pellets in the stellarator TJ-II,” *Nucl. Fusion*, vol. 57, no. 5, pp. 056039–056048, 2017.

[35] J. L. Velasco *et al.*, “Particle transport after pellet injection in the TJ-II stellarator,” *Plasma Phys. Control. Fusion*, vol. 58, no. 8, 2016.

[36] G. Grieger *et al.*, “Physics optimization of stellarators,” *Phys. Fluids B*

Plasma Phys., vol. 4, no. 7, p. 2081, 1992.

[37] G. A. Emmert, R. M. Wieland, A. T. Mense, and J. N. Davidson, "Electric sheath and presheath in a collisionless, finite ion temperature plasma," *Phys. Fluids*, vol. 23, no. 4, p. 803, 1980.

[38] L. Lengyel, V. Rozhanskij, and L. Veselova, "Electrostatic shielding of vaporizing surfaces exposed to hot plasmas," *Nucl. fusion*, vol. 38, no. 12, pp. 1679–1690, 1996.

[39] L. Lengyel, "Pellet ablation in hot plasmas and the problem of magnetic shielding," *Phys. Fluids*, vol. 21, p. 1945, 1978.

[40] A. Matsuyama, B. Pégourié, R. Sakamoto, J. S. Mishra, G. Motojima, and H. Yamada, "Over-ablation and deflection of hydrogen pellets injected into neutral beam injection heated plasmas in the Large Helical Device," *Plasma Phys. Control. Fusion*, vol. 54, no. 3, p. 35007, 2012.

[41] S. P. Hirshman, "Steepest-descent moment method for three-dimensional magnetohydrodynamic equilibria," *Phys. Fluids*, vol. 26, no. 12, p. 3553, 1983.

[42] S. P. Hirshman, K. C. Shaing, W. I. van Rij, C. O. Beasley, and E. C. Crume, "Plasma transport coefficients for nonsymmetric toroidal confinement systems," *Phys. Fluids*, vol. 29, no. 9, pp. 2951–2959, Sep. 1986.

[43] S. P. Hirshman and O. Betancourt, "Preconditioned descent algorithm for rapid calculations of magnetohydrodynamic equilibria," *J. Comput. Phys.*, vol. 96, no. 1, pp. 99–109, Sep. 1991.

[44] F. Castejón *et al.*, "3D effects on transport and plasma control in the TJ-II stellarator," *Nucl. Fusion*, vol. 57, no. 10, 2017.

[45] F. L. Tabarés *et al.*, "Energy and particle balance studies under full boron and lithium-coated walls in TJ-II," *Contrib. to Plasma Phys.*, vol. 50, no. 6–7, pp. 610–615, 2010.

[46] F. L. Tabarés *et al.*, "Plasma performance and confinement in the TJ-II stellarator with lithium-coated walls," *Plasma Phys. Control. Fusion*, vol. 50, no. 12, p. 124051, Dec. 2008.

[47] K. J. McCarthy *et al.*, "The Pellet Injector and Associated Diagnostics for Performing Plasma Studies on the TJ-II Stellarator," in *PoS(ECPD2015)*, 2015, no. April, pp. 1–7.

[48] E. de la Cal *et al.*, "The Visible Intensified Cameras for Plasma Imaging in the TJ-II Stellarator," *Contrib. to Plasma Phys.*, vol. 51, no. 8, pp. 742–753, Sep. 2011.

[49] N. Panadero, K. J. McCarthy, E. de la Cal, J. H. Sánchez, R. García, and M. Navarro, "Observation of Cryogenic Hydrogen Pellet Ablation with a Fast-frame Camera System in the TJ II Stellarator," in *ECA Vol. 40A*, 2016, pp. 6–9.

[50] K. J. McCarthy, “Diagnostic tools for probing hot magnetically confined plasmas,” in *PUBLiCan, ediciones de la Universidad de Cantabria IV*, 2011, pp. 65–67.

[51] J. Herranz, F. Castejón, I. Pastor, and K. J. McCarthy, “The spectrometer of the high-resolution multiposition Thomson scattering diagnostic for TJ-II,” *Fusion Eng. Des.*, vol. 65, no. 4, pp. 525–536, 2003.

[52] T. S. Pedersen *et al.*, “Confirmation of the topology of the Wendelstein 7-X magnetic field to better than 1:100,000,” *Nat. Commun.*, vol. 7, p. 13493, 2016.

[53] T. Klinger *et al.*, “Performance and properties of the first plasmas of Wendelstein 7-X,” *Plasma Phys. Control. Fusion*, vol. 59, no. 1, p. 14018, 2017.

[54] C. Beidler *et al.*, “Physics and Engineering design for Wendelstein 7-X,” *IPP 2/300 Rep.*, p. 38, 1989.

[55] R. C. Wolf, “A stellarator reactor based on the optimization criteria of Wendelstein 7-X,” *Fusion Eng. Des.*, vol. 83, no. 7–9, pp. 990–996, 2008.

[56] V. Erckmann *et al.*, “Electron Cyclotron Heating for W7-X: Physics and Technology,” *Fusion Sci. Technol.*, vol. 52, no. 2, pp. 291–312, Aug. 2007.

[57] P. McNeely *et al.*, “Current status of the neutral beam heating system of W7-X,” *Fusion Eng. Des.*, vol. 88, no. 6–8, pp. 1034–1037, Oct. 2013.

[58] J. Ongena *et al.*, “The dedicated ICRH system for the stellarator Wendelstein 7-X,” in *AIP Conference Proceedings*, 2014, pp. 105–112.

[59] T. Sunn Pedersen *et al.*, “Plans for the first plasma operation of Wendelstein 7-X,” *Nucl. Fusion*, vol. 55, no. 12, p. 126001, 2015.

[60] M. Dibon *et al.*, “Blower Gun pellet injection system for W7-X,” *Fusion Eng. Des.*, vol. 98–99, pp. 1759–1762, 2015.

[61] C. A. Foster, R. J. Colchin, S. L. Milora, K. Kim, and R. J. Turnbull, “Solid hydrogen pellet injection into the Ormak tokamak,” *Nucl. Fusion*, vol. 17, no. 5, pp. 1067–1075, 1977.

[62] H. W. Müller *et al.*, “High β plasmoid formation, drift and striations during pellet ablation in ASDEX Upgrade,” *Nucl. Fusion*, vol. 42, no. 3, pp. 301–309, 2002.

[63] B. P. Van Milligen *et al.*, “A global resonance phenomenon at the TJ-II stellarator,” *Nucl. Fusion*, vol. 51, p. 13005, 2011.

[64] F. Medina, M. A. Ochando, A. Baciero, and J. Guasp, “Characterization of ripple-trapped suprathermal electron losses by their bremsstrahlung emission in the soft x-ray range at the TJ-II stellarator,” *Plasma Phys. Control. Fusion*, vol. 49, pp. 385–394, 2007.

[65] M. Landreman, H. M. Smith, A. Mollén, and P. Helander, “Comparison of

particle trajectories and collision operators for collisional transport in nonaxisymmetric plasmas," *Phys. Plasmas*, vol. 21, no. 4, p. 42503, Apr. 2014.

[66] R. Sakamoto and H. Yamada, "Observation of cross-field transport of pellet plasmoid in LHD," *Plasma Fusion Res.*, vol. 6, no. 2011, pp. 1–5, 2011.

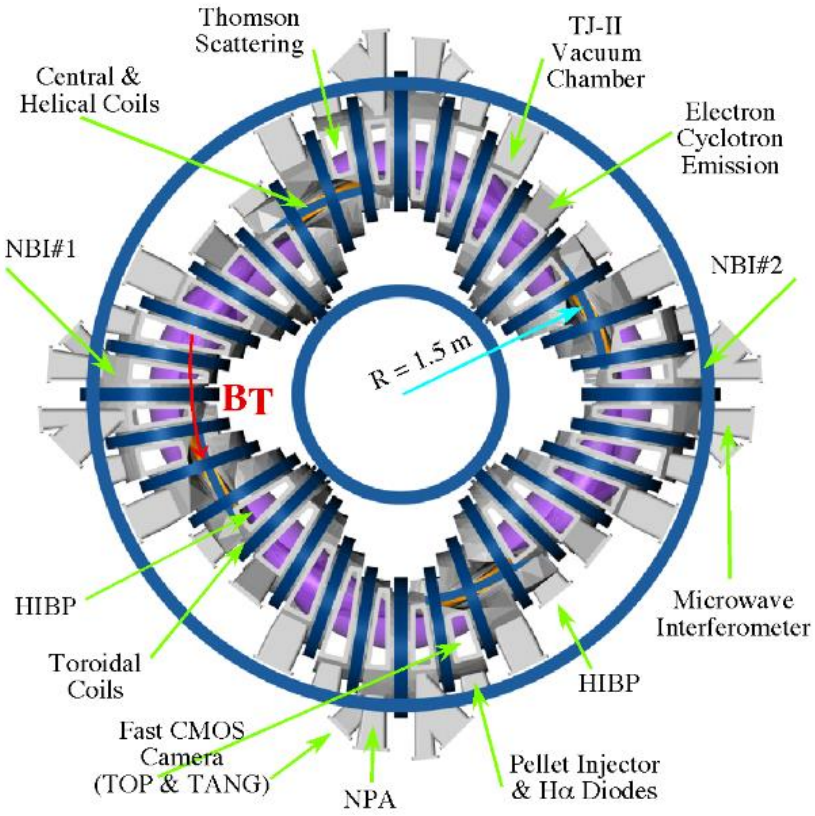

Figure 1. Bird's eye view of the TJ-II. The locations of the magnetic coils, PI, associated diagnostic and relevant plasma diagnostics are highlighted.

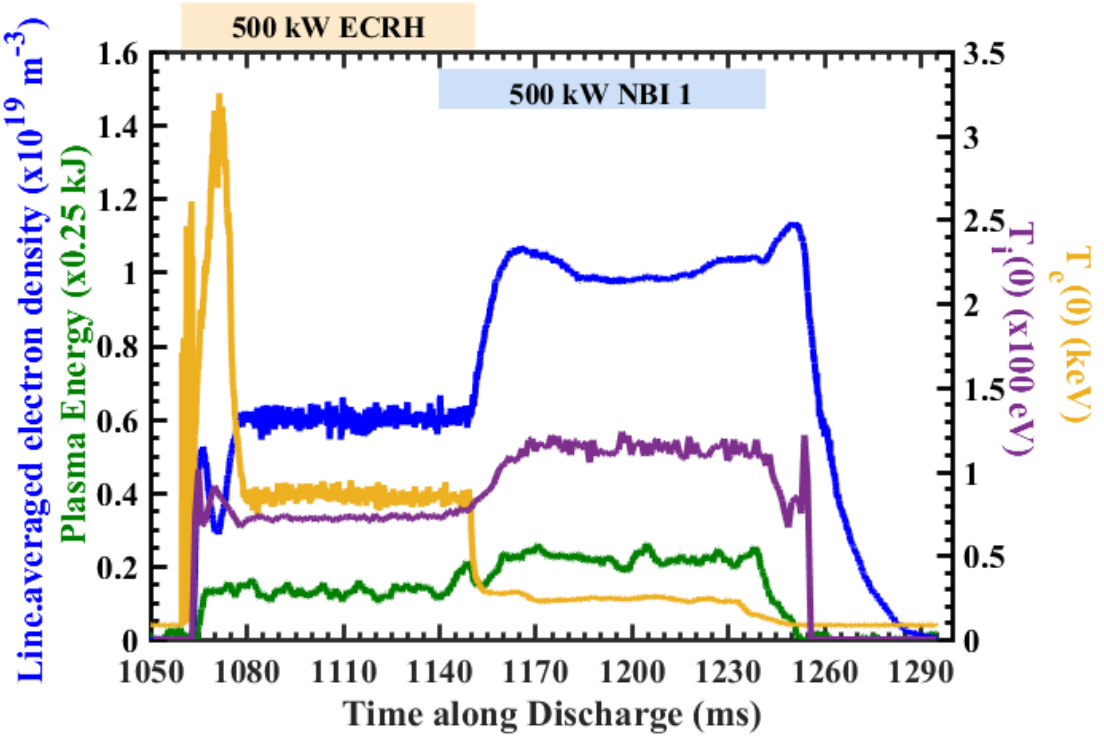

Figure 2. An ECRH and NBI heated plasma TJ-II discharge (#44585) showing the evolution of the line-averaged electron density (blue) and plasma energy (green), plus central electron (orange) and majority ion (purple) temperatures. Note: the ECE signal does not reflect the true $T_e(0)$ during the high density NBI phase.

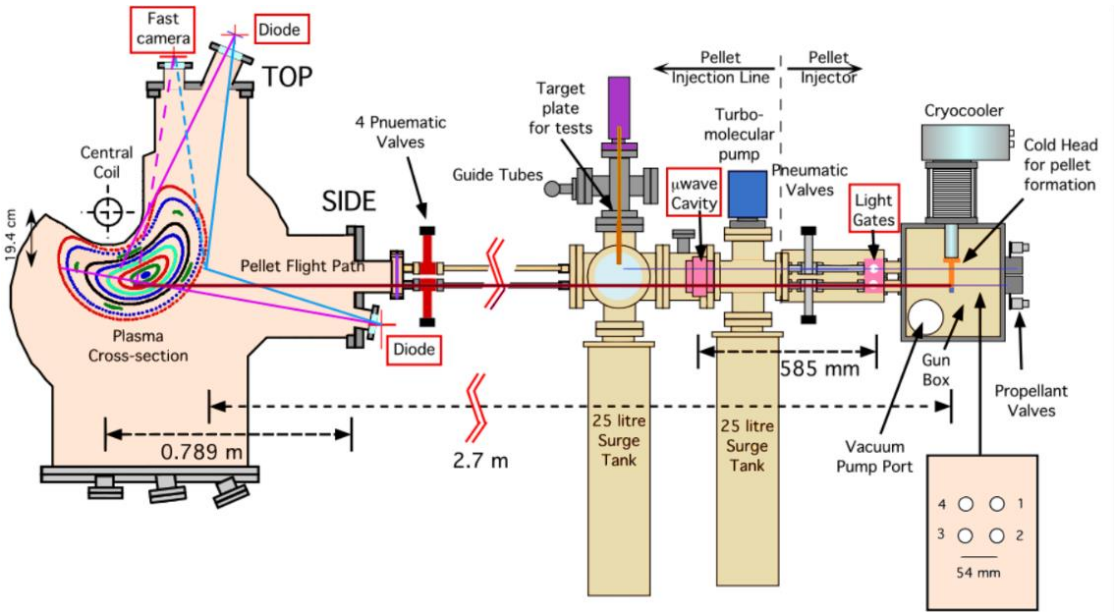

Figure 3 Cross-sectional sketch of the TJ-II vacuum chamber, magnetic surfaces, and the pellet injector. The relative locations of pellet Lines#1 through #4 are indicated with respect to the rear of the PI.

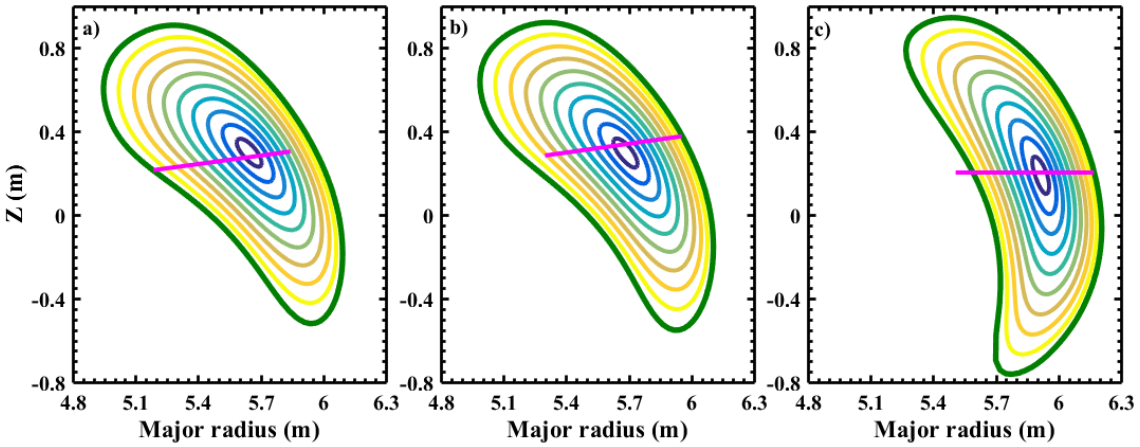

Figure 4. Plasma cross-sections for three W7-X injection ports a) AEL41 (ϕ = - 2.22 rad); b) AEK41 (ϕ = - 2.24 rad), and c) AEE41 (ϕ = - 2.39 rad). Pellet injection flight paths are shown in magenta (the injection angles are 0.13 rad for AEL41, -3.0 rad for AEK41, and π rad for AEE41).

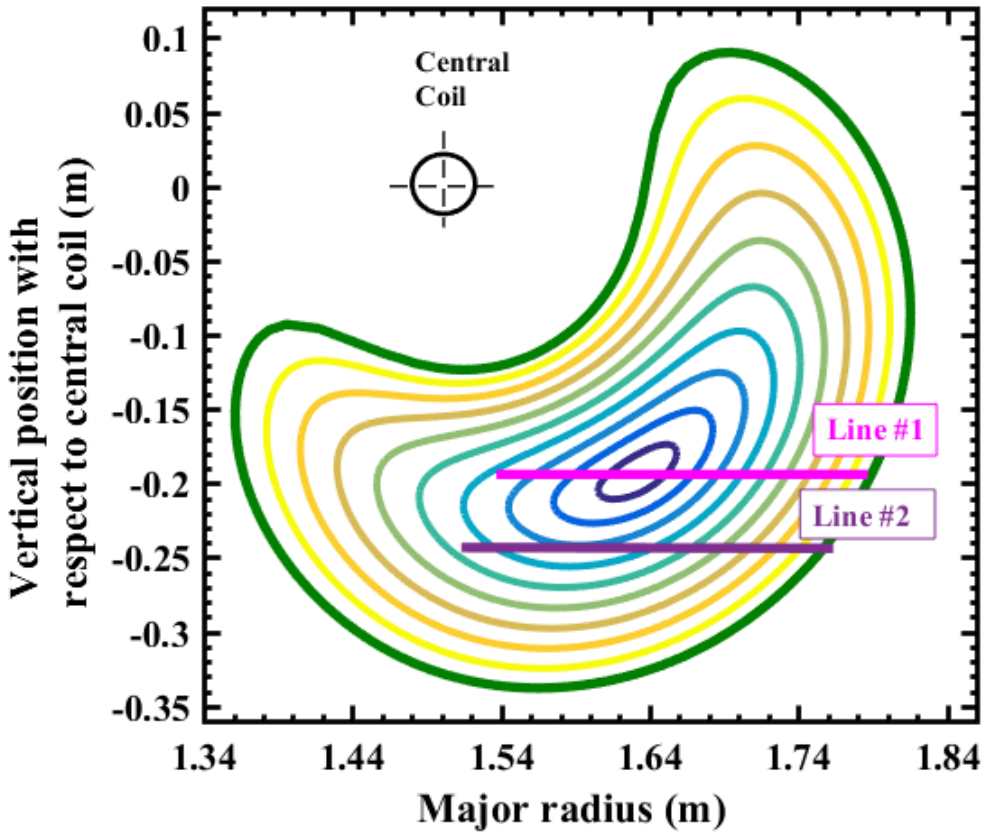

Figure 5. Closed magnetic flux surfaces of the 100-44-64 magnetic configuration for toroidal angle, ϕ, 14º. Pellet flight paths through the plasma for injection lines #1 and #2 are shown.

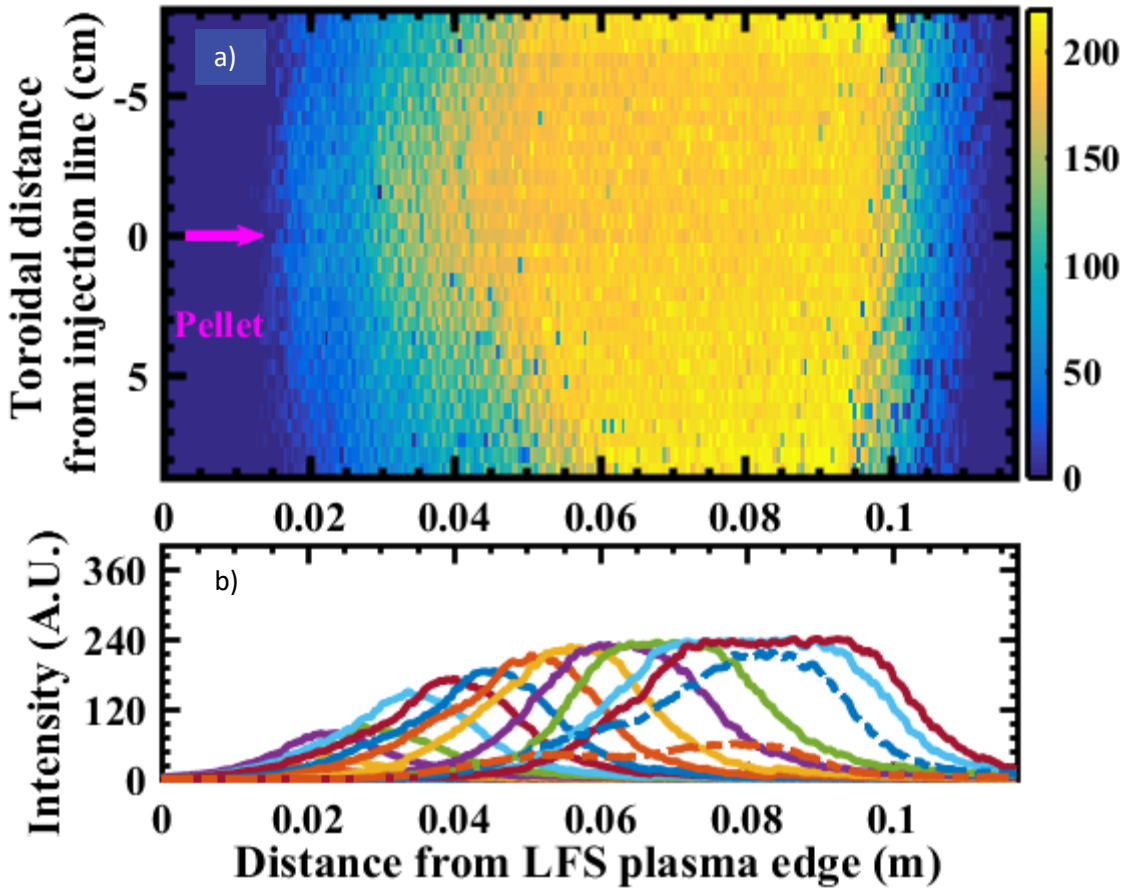

Figure 6. a) Montage of snap-shot images for discharge #44624 when a pellet with 6.2×10^{18} H atoms was injected along Line#1 at 912 ± 18 m/s (frame rate is 150 kfps, exposure time is ~ 4.1 μs). b) Radial light profiles for collected frames (the dashed profiles correspond to the drifting plasmoid that remains after pellet has been completely ablated).

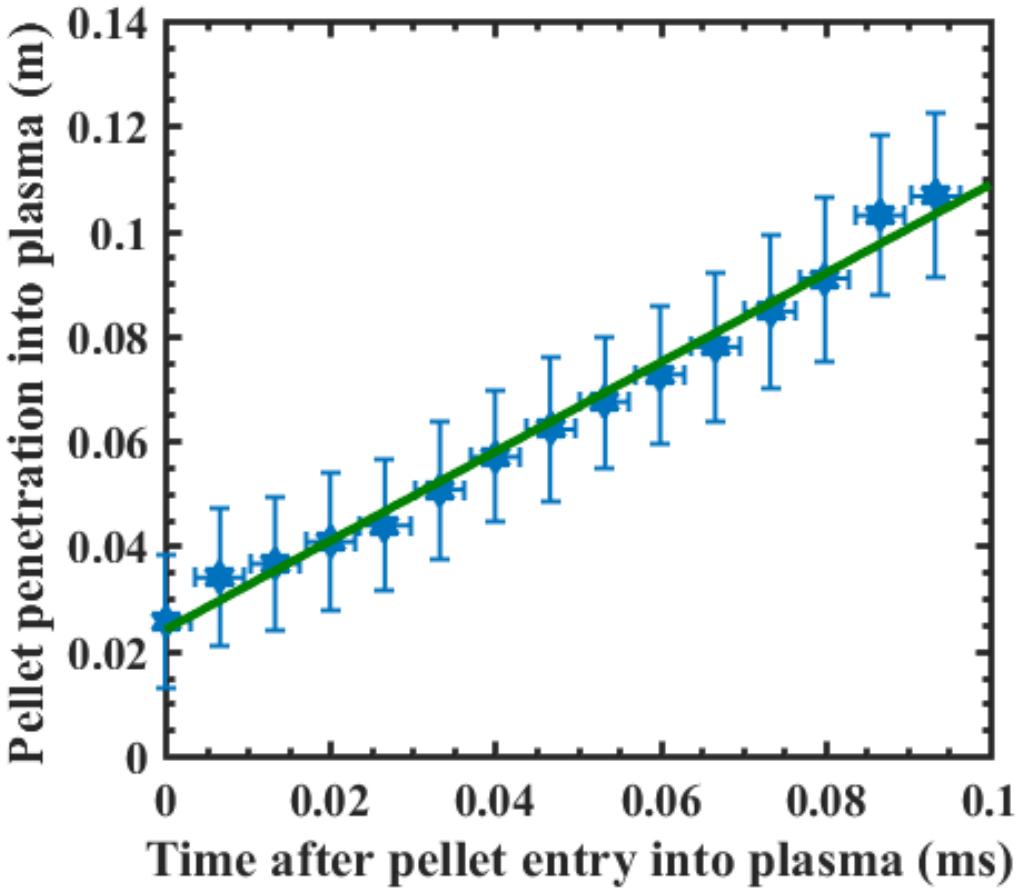

Figure 7. Pellet radial position (obtained from fast-camera images) versus time after pellet entry into discharge #44624. It is assumed that the pellet is located at maximum light intensity. The estimated velocity is 849 ± 20 m/s. Although snap-shot images corresponding to end of pellet lifetime are saturated, error bars are not significantly affected. This is because of the uncertainty in the camera calibration and, hence, in the pixel-meter equivalence, which is the principal contributor to calculated uncertainties.

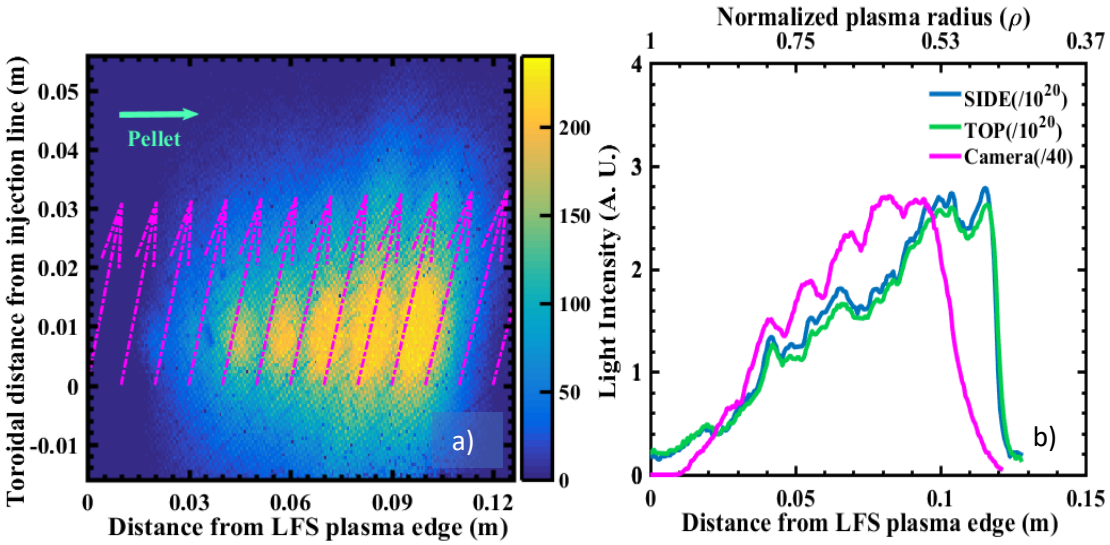

Figure 8. at) Montage of snap-shot images (frame rate = 52.5 kfps, exposure time ~ 4.1 μs) taken from the INNER TOP viewport versus distance into the plasma (the injection and magnetic field directions are indicated) at $\phi = 14^{o}$. b) H_{α} emissions detected by the SIDE (blue) and TOP (green) photodiodes, plus the light profile obtained from the fast camera (magenta), versus distance into plasma. Both figures are for a pellet with 1.2×10^{19} H atoms injected into discharge #44828 at 682 m/s along Line#1 during the ECRH phase.

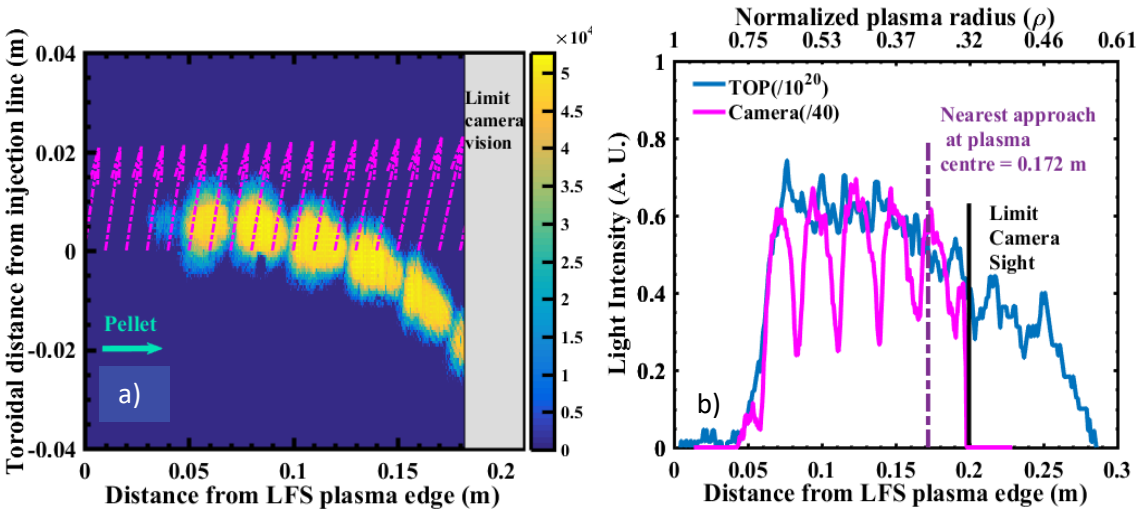

Figure 9. a) Montage of snap-shot images (frame rate = 37.5 kfps, exposure time ~26.7 μs) taken from the INNER TOP viewport versus distance into the plasma (the injection and magnetic field directions are indicated) at $\phi = 14^{o}$. b) H_{α} emissions detected by the TOP (blue) photodiode, plus the light profile obtained from the fast camera (magenta), versus distance into plasma. Both figures are for a pellet with 6.5×10^{18} H atoms injected into discharge #41391 at 1009 m/s along Line#2 during an unbalanced NBI heating phase.

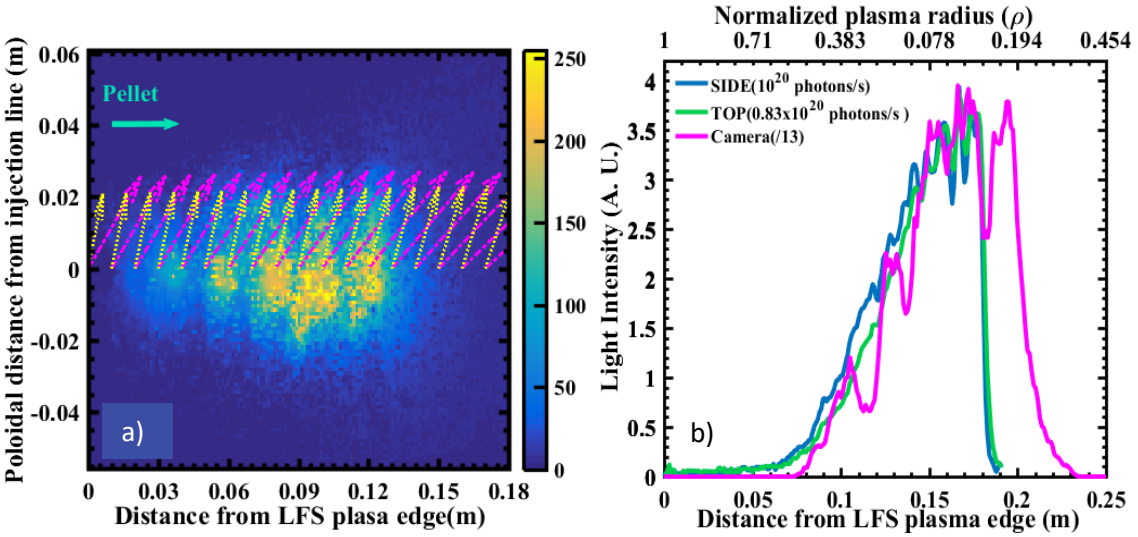

Figure 10. a) Montage of snap-shot images (frame rate = 63 kfps, exposure time ~2μs) taken from the TANG viewport versus distance into the plasma (the injection and magnetic field directions are indicated) at $\phi = 14^{o}$. b) H_{α} emissions detected by the SIDE (blue) and TOP (green) photodiodes, plus the light profile obtained from the fast camera (magenta), versus distance into plasma. Both figures are for a pellet with 9.4×10^{18} H atoms injected into discharge #45110 at 1000 m/s along Line #1 during the ECRH heating phase.

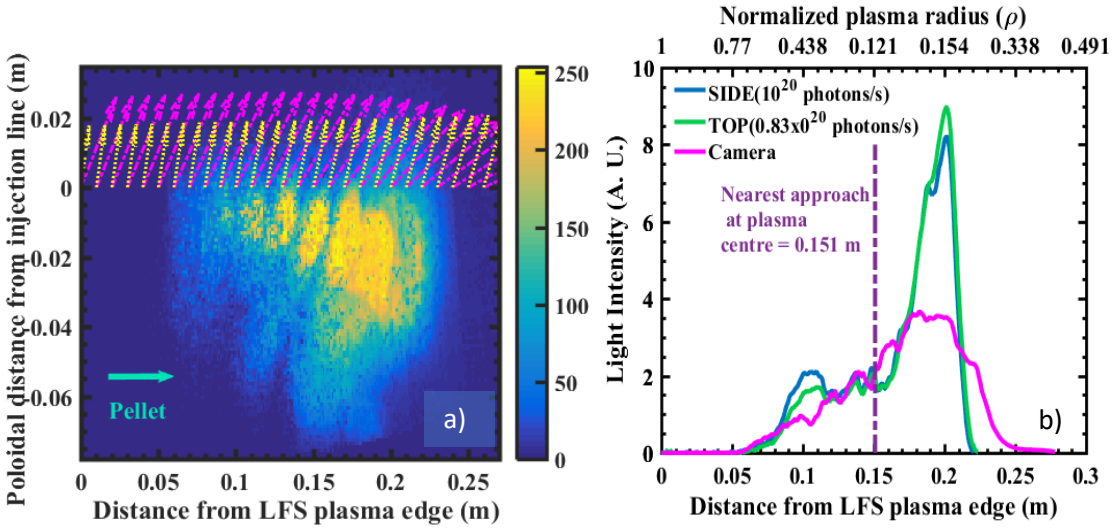

Figure 11. a) Montage of snap-shot images (frame rate = 63 kfps, exposure time ~2 μs) taken from the TANG viewport versus distance into the plasma (the injection and magnetic field directions are indicated) at $\phi = 13^{o}$. b) H_{α} emissions detected by the SIDE (blue) and TOP (green) photodiodes, plus the light profile obtained from the fast camera (magenta), versus distance into plasma. Both figures are for a pellet with 1.4×10^{19} H atoms injected into discharge #45091 at 1009 m/s along Line #4 during an unbalanced NBI#1 heating phase.

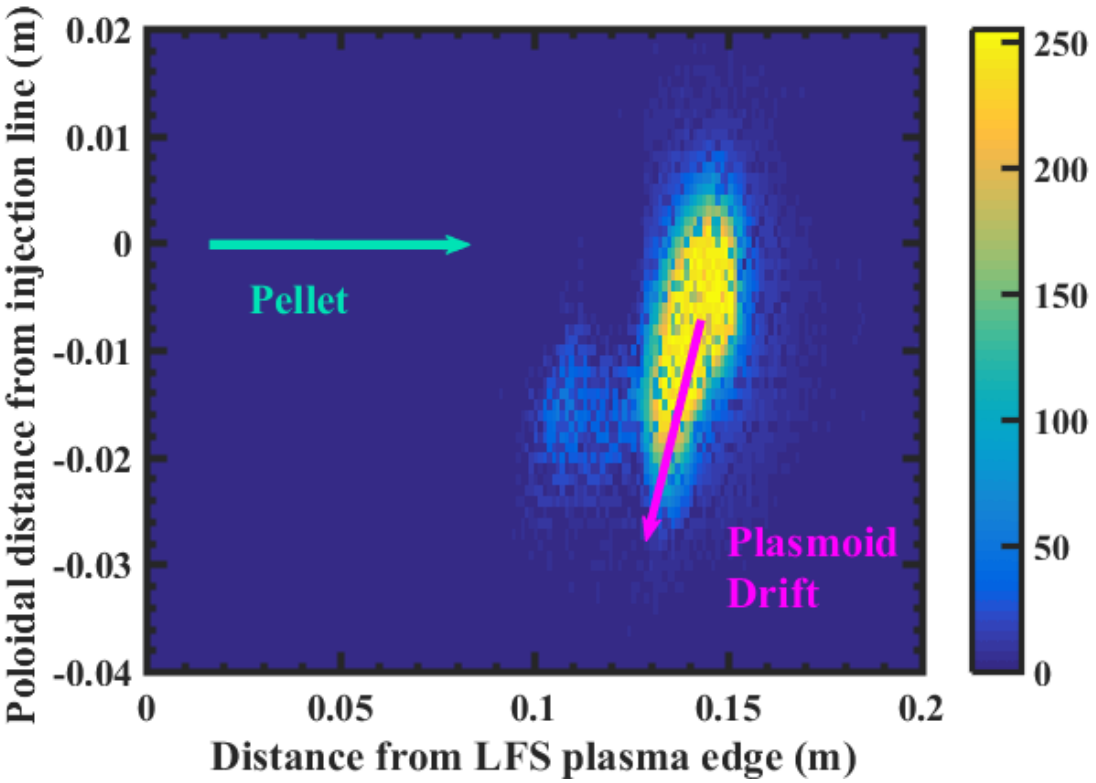

Figure 12. Snap-shot images (frame rate = 63 kfps, exposure time ~2 μs) taken from the TANG viewport versus distance into the plasma (the injection direction is indicated) at $\phi = 13^{o}$ for a pellet with 1.06×10^{19} H atoms injected into discharge #45110 at 932 m/s along Line #4 during an almost balanced NBI heating phase. Plasmoid drift towards the lower LFS of the plasma can be appreciated.

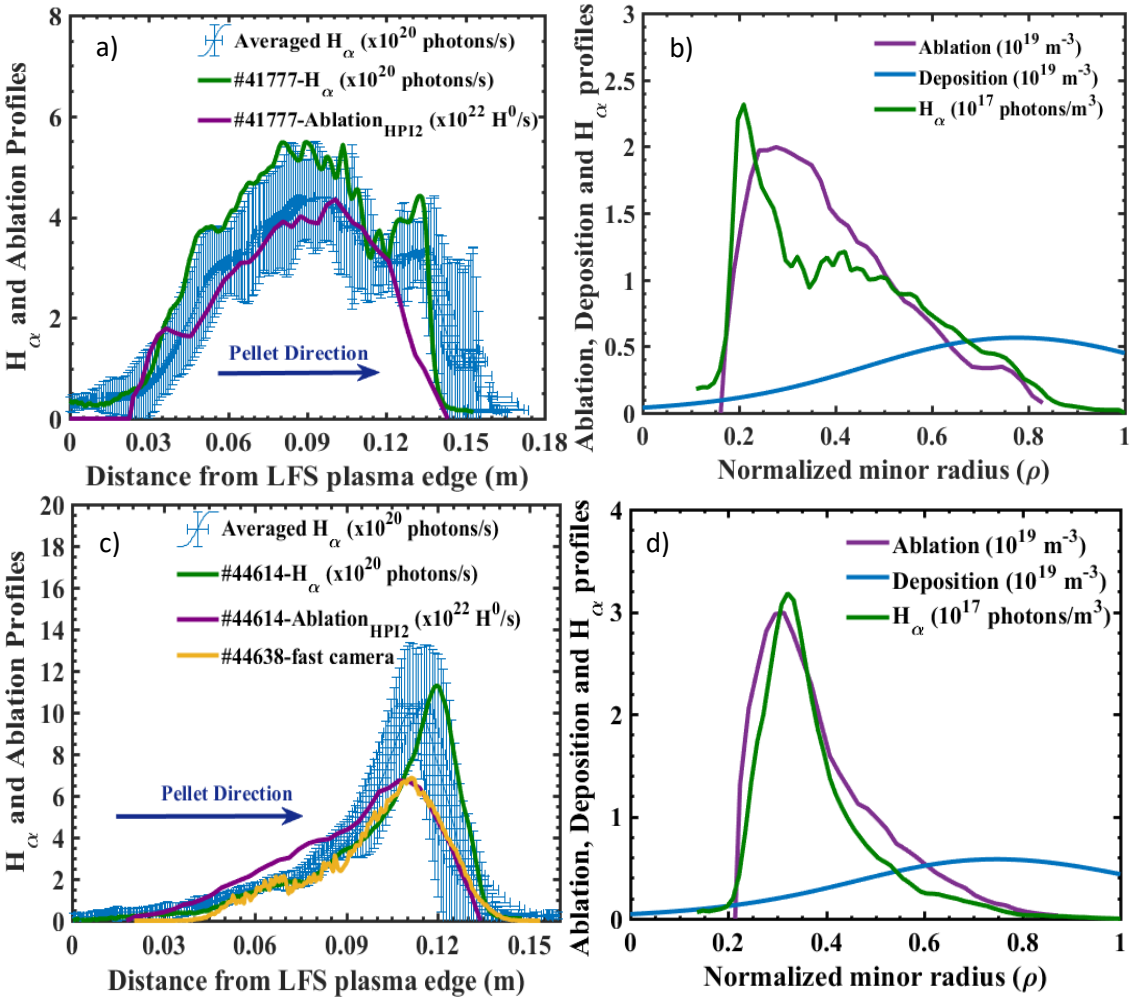

Figure 13. HPI2 simulated ablation (purple) and deposition (blue) profiles compared with measured H_α emission profiles (green) for pellet#2 injected along Line #1 into the ECRH phase of discharges a) and b) #41777 ($6.1x10^{18}$ H atoms, velocity = 808 m/s) and c) and d) #44614 ($6.6x10^{18}$ H^0, velocity = 900 m/s). Figures a) and c) show experimental H_α emission in photons/s, together with the average emission and the dispersion for a number of reproducible discharges; ablation profile is shown here in H^0 atom/s. In addition, c) shows, in yellow, the light emission profile obtained from the montage of snap-shots images from fast camera for #44738 (from the series of reproducible discharges). On the other hand, b) and d) show ablation and deposition profiles in m^{-3}, compared to H_α emission in photons/m^3.

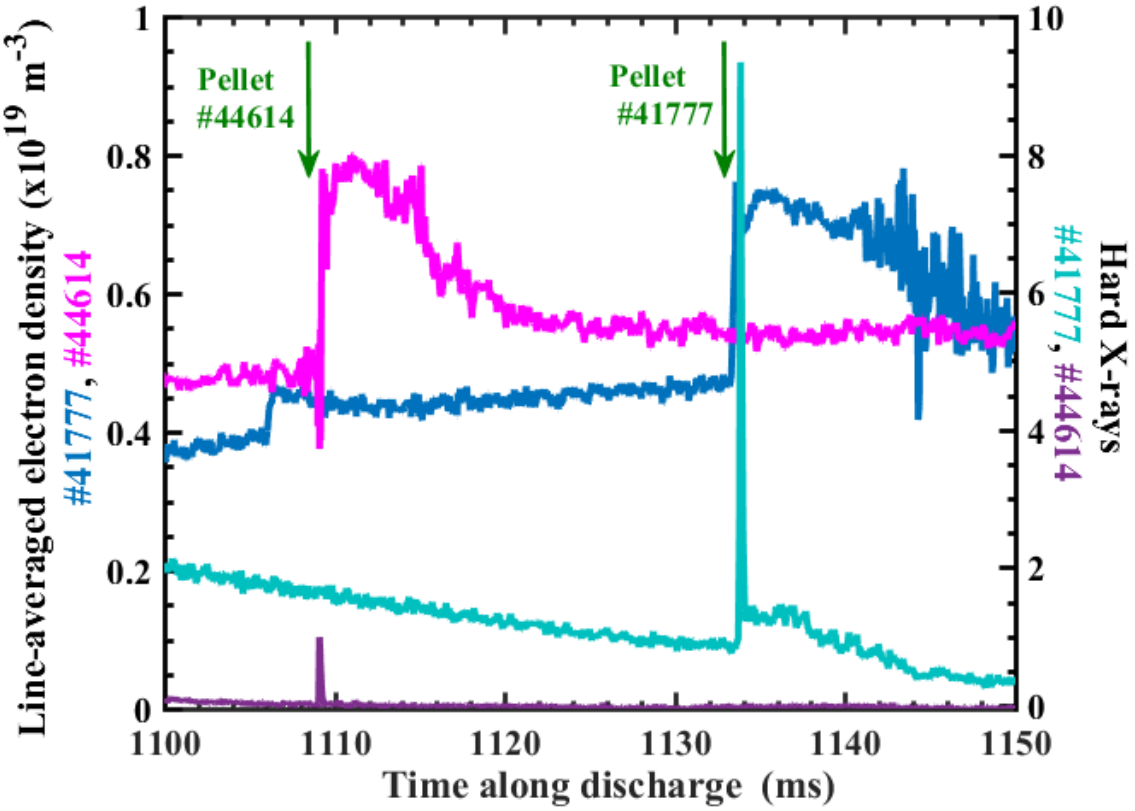

Figure 14. Hard X-ray emission for discharges #41777 (sky blue) and #44614 (purple). The line-averaged densities of both discharges (dark blue for #41777 and magenta for #44614) are also shown to facilitate the identification of pellet injection time.

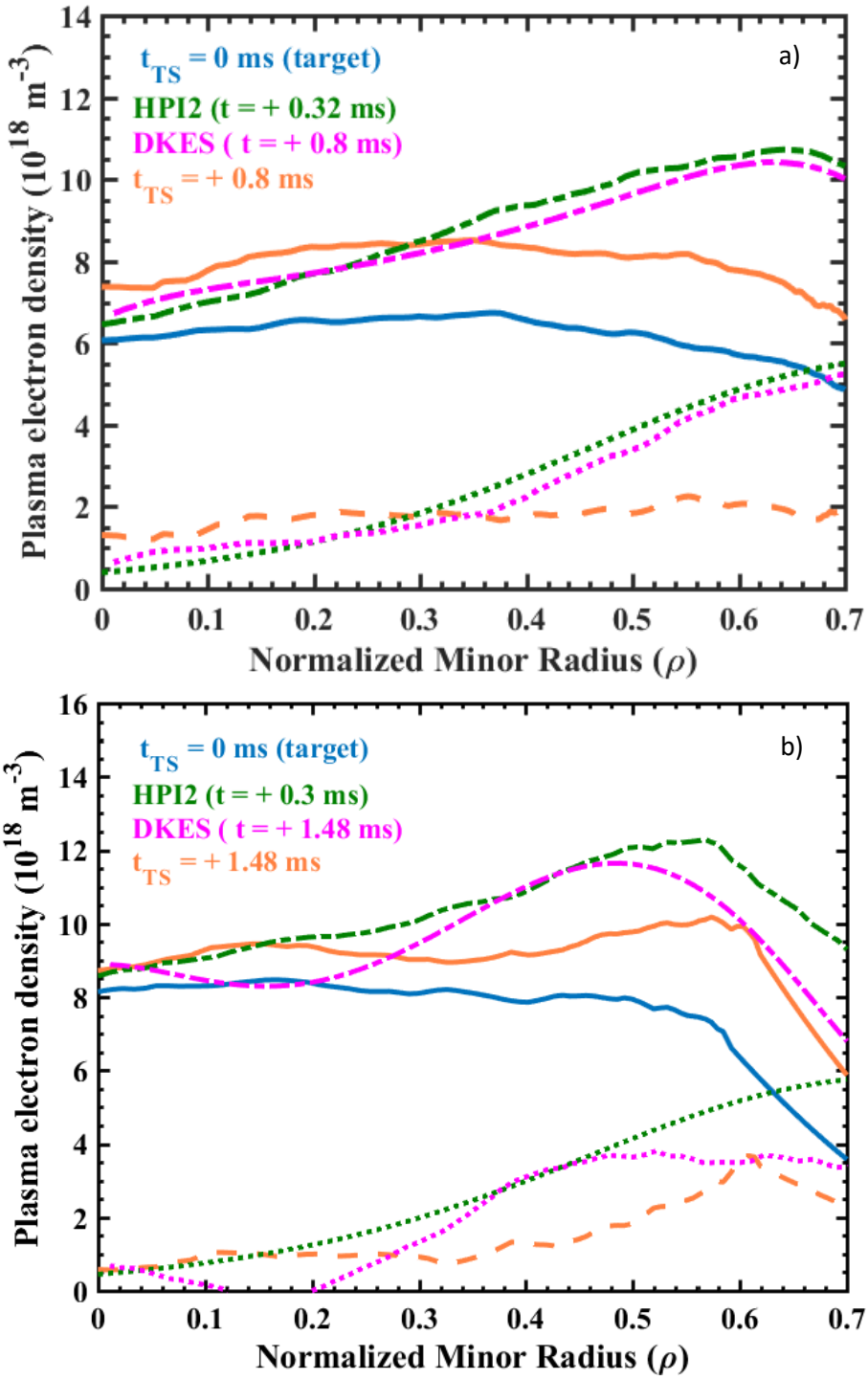

Figure 15. TS electron density profiles measured before (solid blue) and after an injection (solid orange) plus density profiles obtained with HPI2 code (dashed/dotted green) and DKES (dashed/dotted magenta). The corresponding electron density increases are also shown (orange dashed lines for TS measurements, green dotted line for HPI2 simulations and magenta dotted lines for DKES simulations). a) discharge #41777 (6.1×10^{18} H^0, velocity = 808 m/s) and b) discharge #44614 (6.6×10^{18} H^0, velocity = 900 m/s).

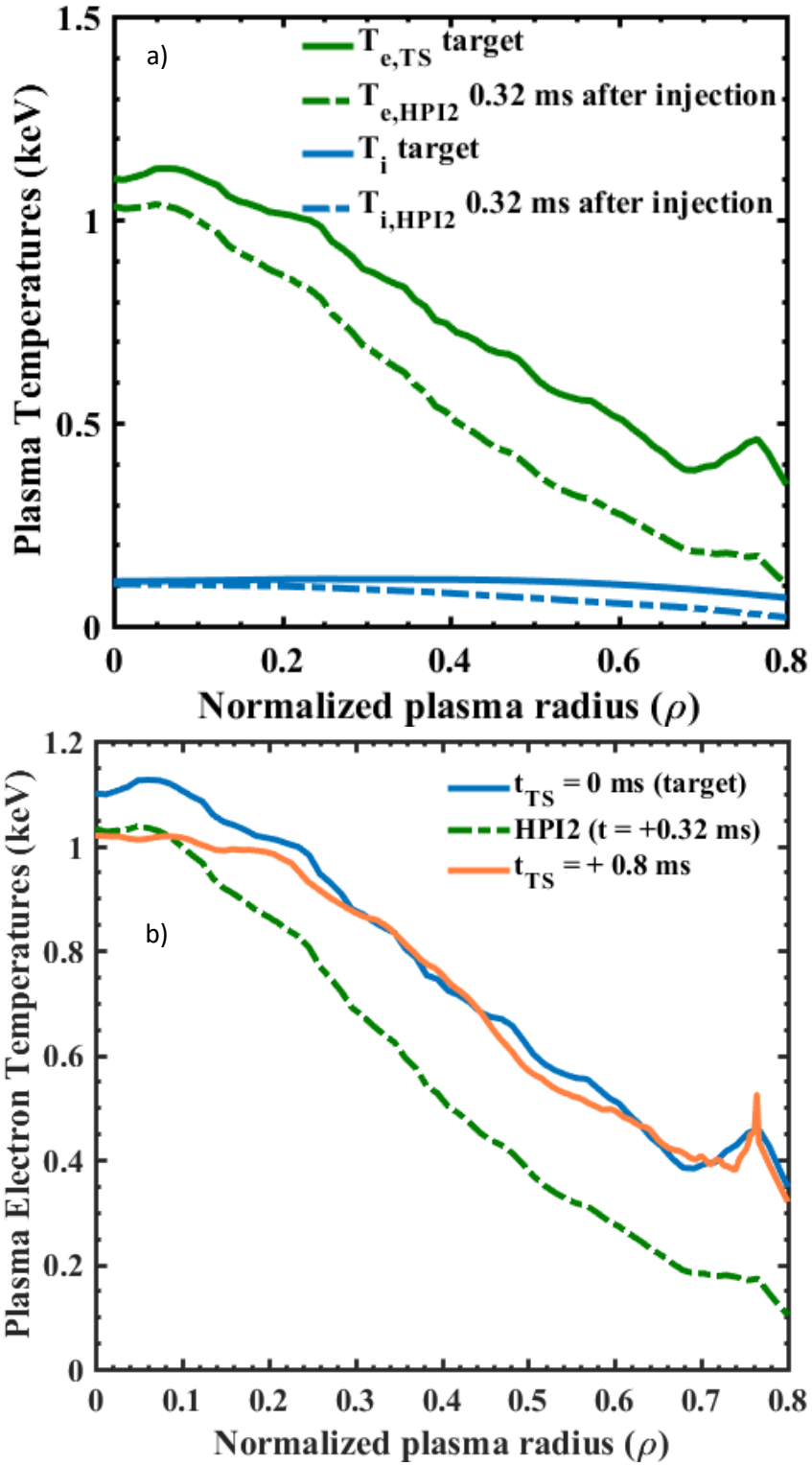

Figure 16. a) Target plasma electron (green) and ion (blue) temperature profiles before (solid, experimental) and after (dash-dotted lines, predicted) complete pellet ablation and homogenization for discharge #41777 (6.1×10^{18} H^0, velocity = 808 m/s). b) Electron temperature profiles of the target plasma (blue) and after pellet injection (green). The HPI2 simulated electron temperature profile (dashed/dotted light green) is also shown.

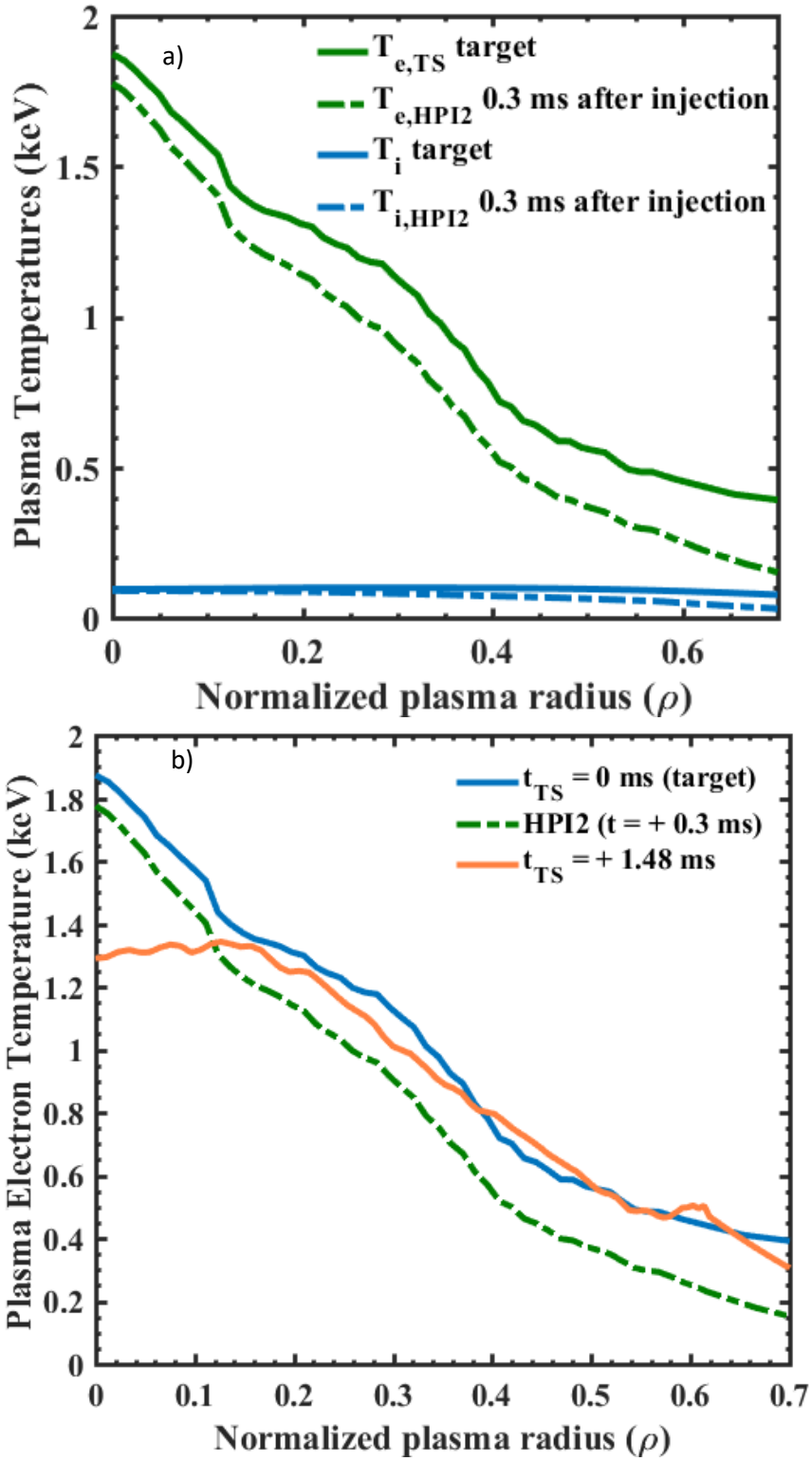

Figure 17 . a) Electron (green) and ion (blue) temperature profiles before (solid, experimental) and after (dash-dotted lines, predicted) complete pellet ablation and homogenization for discharge #44614 (6.6×10^{18} H0, velocity = 900 m/s). b) Electron temperature profiles of the target plasma (blue) and after pellet injection (green). A HPI2 simulated electron temperature profile (dashed/dotted light green) is also shown.

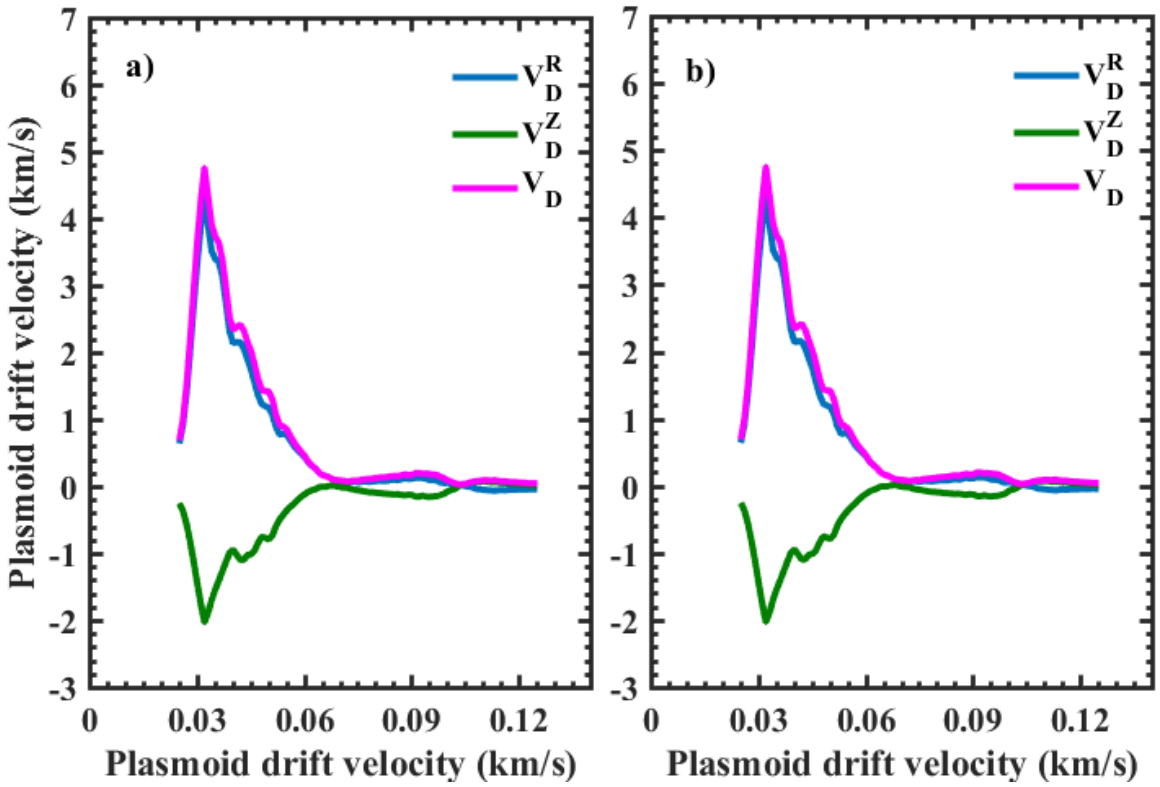

Figure 18. Simulated evolution of the plasmoid drift velocity, during the homogenization phase, in the radial (blue) and poloidal (green) directions plus the total (pink) for plasmoid #12 (originating at $\rho \sim 0.8$) for discharges a) #41777 and b) #44614.

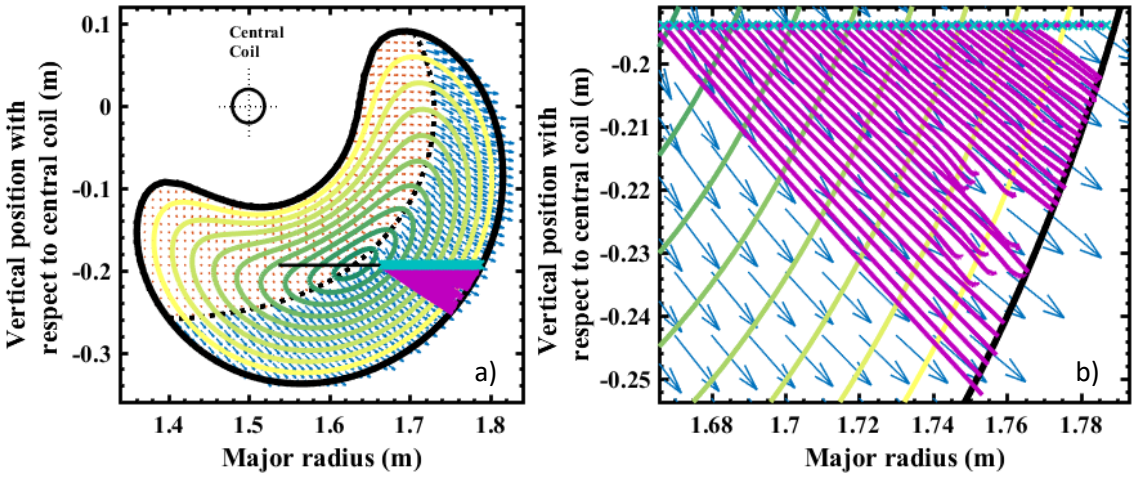

Figure 19. a) Effective inverse curvature radius vector field for the TJ-II standard configuration, $\phi = 14^{o}$, and plasmoid of dimension parallel to magnetic field lines, Z_0, of 0.8 m. Dotted black line separates regions of positive (upper left of curve) and negative inverse curvature radius (lower right of curve). b) Close-up of plasma cross-section showing blue arrows that represent outwards effective drift. The trajectories of all plasmoids for the simulation of #41777 are shown (purple). Arrow lengths are proportional to plasmoid drift acceleration.

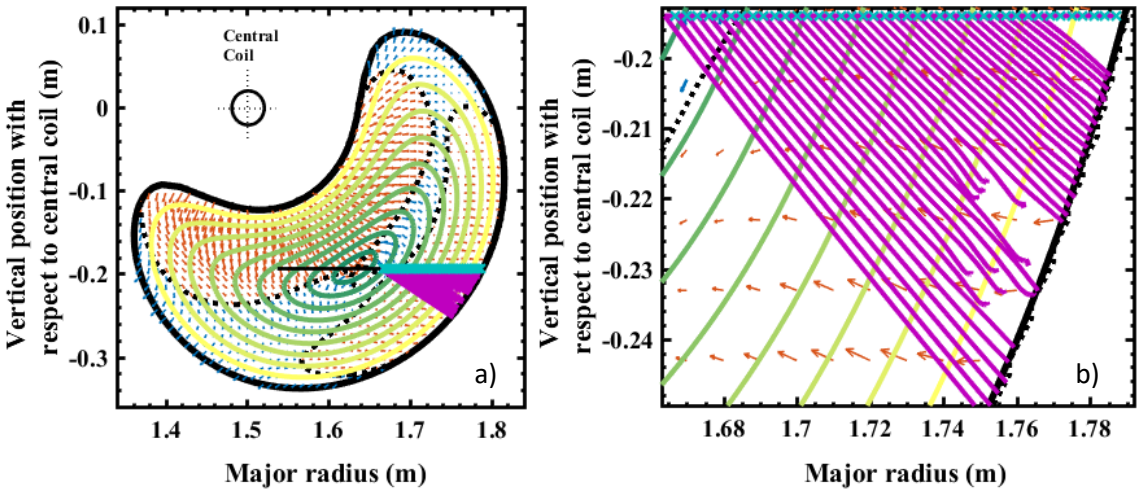

Figure 20. a) Effective inverse curvature radius vector field for the TJ-II standard configuration, $\phi = 14^{o}$, and plasmoid parallel length $Z_0 = 10$ m (red arrows represent inwards effective drift (negative inverse curvature radius), whereas the blues represent outwards (positive inverse curvature radius). Dotted black lines separate regions of positive and negative inverse curvature radius. b) Close-up of plasma cross-section showing the trajectories of all plasmoids in the simulation for discharge #41777 (purple). Arrow lengths are proportional to plasmoid drift acceleration.

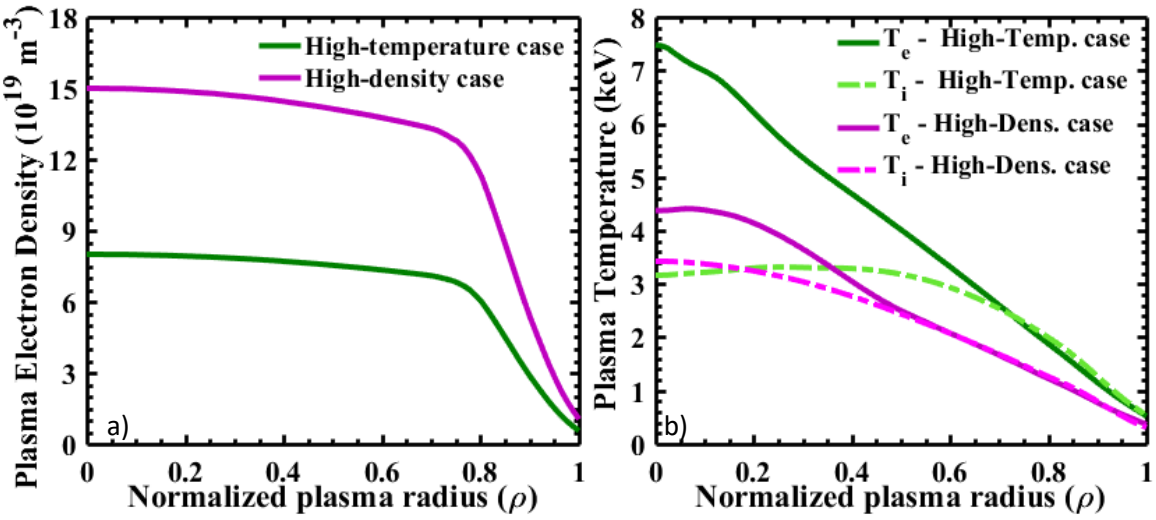

Figure 21. Profiles of at) electron density and b) electron and ion temperature, corresponding to high-temperature (ECRH in X2-Mode) and high-density (ECRH in O2-Mode) scenarios in W7-X.

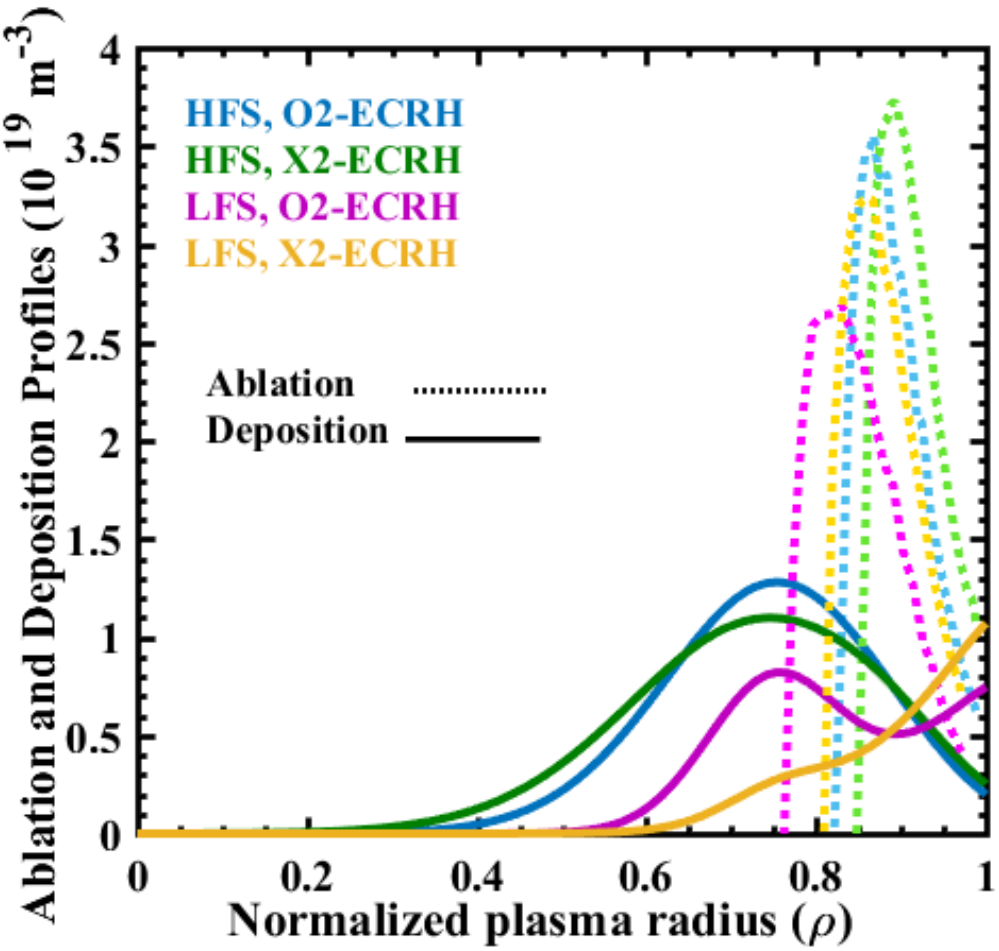

Figure 22. Ablation (dotted) and deposition (solid) profiles for HFS and LFS injections into high-density, low-temperature, plasmas of W7-X (blue is HFS-injection into ECRH-O2 mode heated plasma, green is HFS-injection into ECRH-X2 mode, purple is LFS-injection into ECRH-O2 mode, and yellow is LFS-injection into ECRH-X2 mode). In all cases pellet velocity is 250 m/s, pellet content is 1.9×10^{20} H atoms (length = 2 mm, diameter = 1.5 mm).

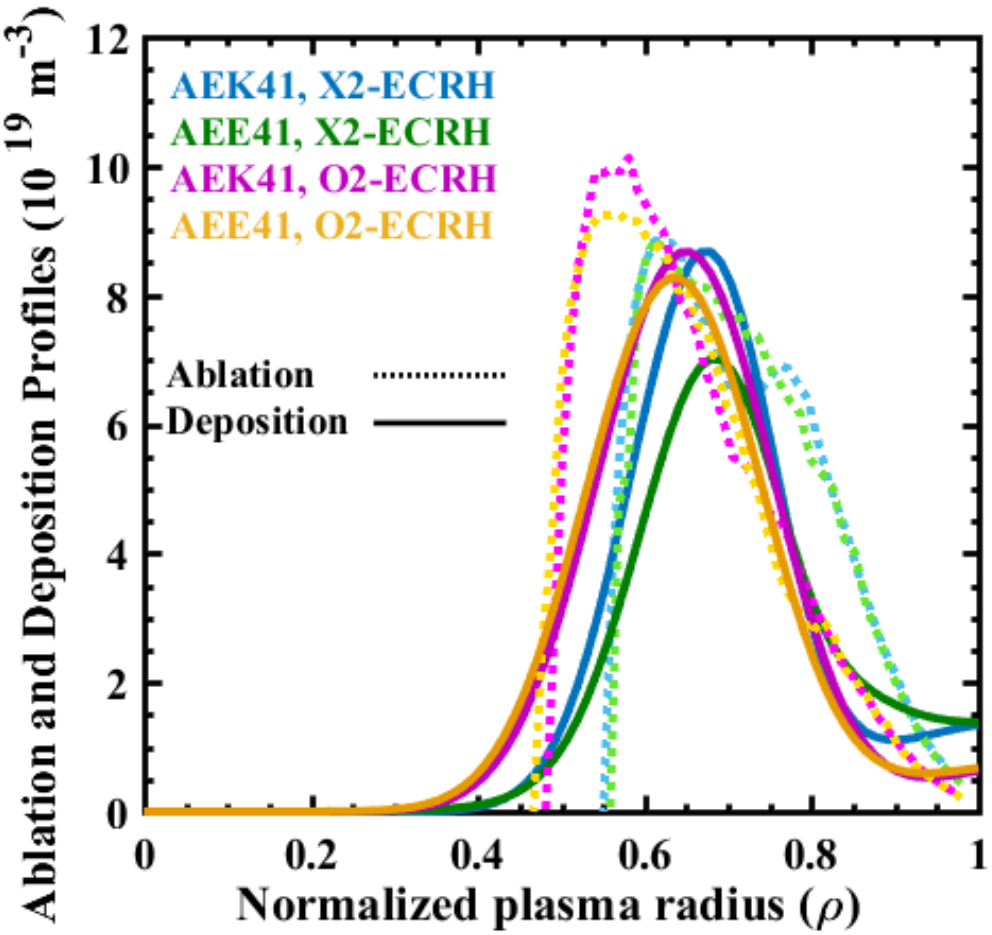

Figure 23. Ablation dotted) and deposition (solid) profiles for 3 mm pellet (diameter = 2.8 mm, pellet content = 8.9×10^{20} H atoms) injected at 600 m/s into high-density, low-temperature, W7-X plasmas from the AEK41 and AEE41 ports (blue is from AEK41 into ECRH-X2 mode, green is from AEE41 into ECRH-X2 mode, purple is injection from AEK41 into ECRH-O2 mode, and yellow is injection from AEE41 into ECRH-O2 mode heated plasmas).

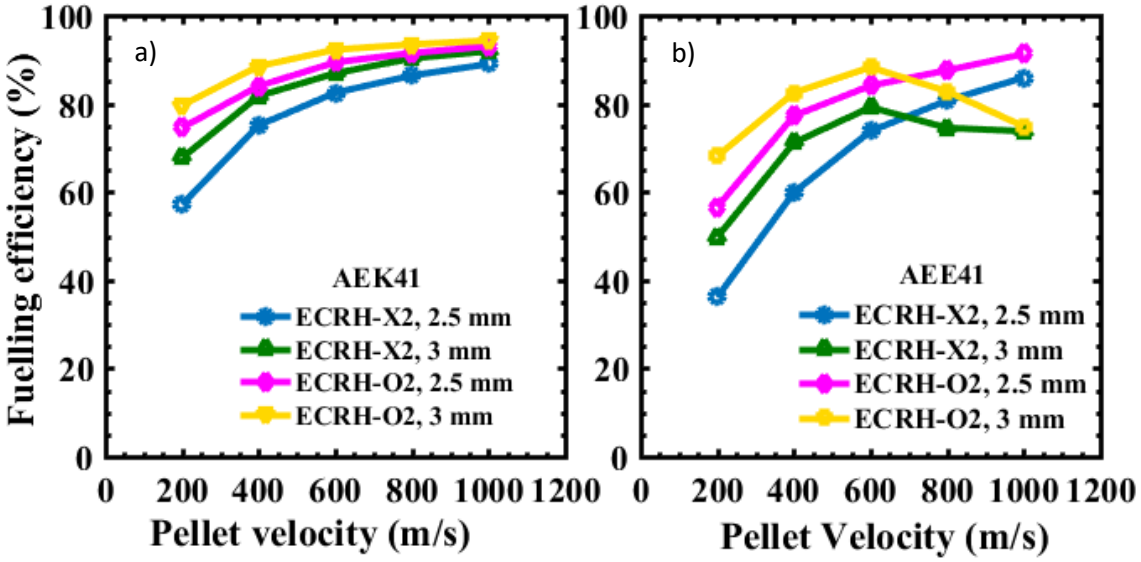

Figure 24. Predicted fuelling efficiencies for injections for series 1 (blue circles- 2.5 mm pellets into X2-mode ECR-heated plasma), series 2 (green triangles- 3 mm pellets into X2-mode ECR-heated plasma), series 3 (pink diamonds- 2.5 mm pellets into O2-mode ECR-heated plasma) and series 4 (yellow squares- 3 mm pellets into O2-mode ECR-heated plasma) from ports a) AEK41 and b) AEE41 for a range of injection velocities (from 200 to 1000 m/s).

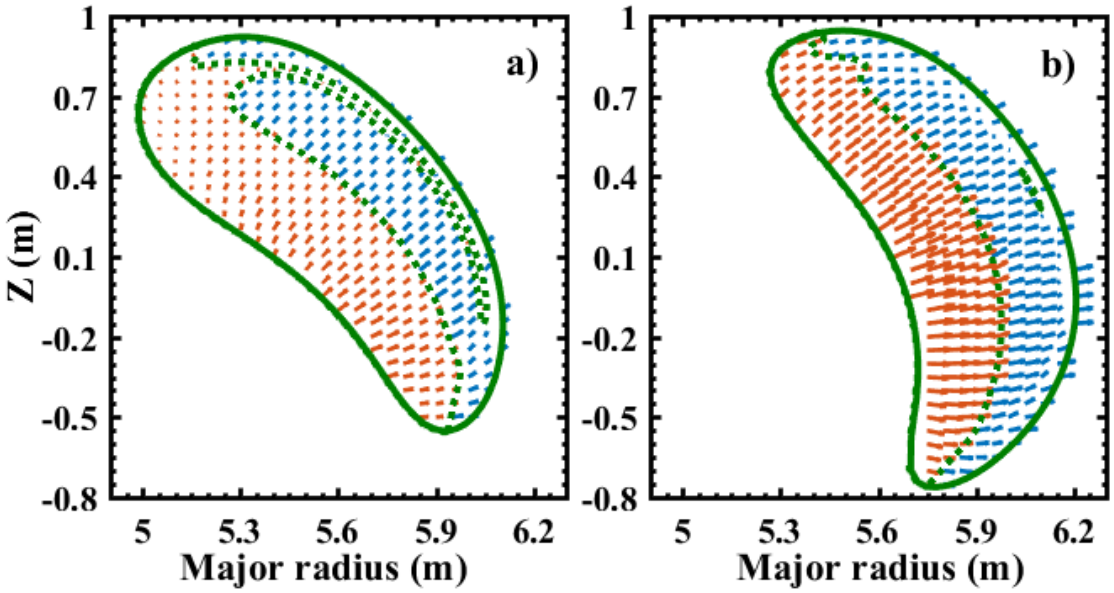

Figure 25. Effective inverse curvature radius vector fields for W7-X injection ports a) AEK41 and b) AEE41 for a plasmoid parallel length of $Z_0 = 0$ m. Red arrows represent inwards effective drift (negative inverse curvature radius), whereas blue arrows represent outwards drift (positive inverse curvature radius); dotted green lines separate regions of positive and negative inverse curvature radius.

Injection port	Heating method	ρ penetration	ρ deposition	$\Delta n_{e,\,max}$	ρ of $\Delta n_{e,max}$	Fueling efficiency (%)
AEL41	ECRH-O2	0.82	0.33	8.7×10^{18}	0.64	98
AEL41	ECRH-X2	0.85	0.24	1.0×10^{19}	0.69	98
AEK41	ECRH-O2	0.77	0.50	1.7×10^{18}	0.72	47
AEK41	ECRH-X2	0.81	0.60	9.9×10^{17}	0.73	43

Table 1. Relevant HPI2 results for four different scenarios considered for the OP1.2 phase of W7-X. Here, "ρ penetration" represents the radial position to which the pellet penetrates, while "ρ deposition" represents the deepest position reached by deposited material. The next two columns show the density increment for maximum post-injection density and the radial position at which this maximum occurs, respectively. All radial positions are given in normalized minor radius units. In the last column, fueling efficiency is the ratio between the number of particles deposited in the plasma and the number of pellet particles.